TECHNISCHE UNIVERSITÄT WIEN Vienna | Austria

ÉCOLE CENTRALE LYON

Master thesis

Application of deconvolution on the turbulent boundary layer wall pressure spectrum

carried out for the purpose of obtaining the degee
of Master of Science (MSc or Dipl.-Ing. or DI)

submitted at
TU Wien, Faculty of Mechanical and Industrial Engineering
by

Rafael ENGELMANN
Mat. Nr.: 1126038

under the supervision of

Univ.Prof. Christophe Bailly
Centre Acoustique
École Centrale de Lyon

and

Univ.Prof. Dipl.-Ing. Dr.techn. Manfred Kaltenbacher
Institute of Mechanics and Mechatronics
TU Wien

Hiermit erkläre ich an Eides statt, dass ich die vorliegende Arbeit selbstständig und ohne fremde Hilfe verfasst, andere als die angegebenen Quellen und Hilfsmittel nicht benutzt und die aus anderen Quellen entnommenen Stellen als solche gekennzeichnet habe.

Wien, am 12.5.2018 Rafael Engelmann

Danksagung

Von ganzem Herzen möchte ich mich bei meinen Eltern bedanken, die mich immer unterstützt und mir die Möglichkeit gegeben haben diesen Weg zu gehen. Für die Wertschätzung und das Vertrauen, die dadurch erst jene Freude am Lernen ermöglicht haben die mich heute begleitet.

Ich möchte mich auch bei der Republik Österreich für die Finanzierung dieses Studiums bedanken und bei der europäischen Union für die Förderung im Namen des ERASMUS Programms.

Abstract

Turbulent boundary layer cross-spectral data has recently been measured for different velocities at zero pressure gradient. The obtained wavenumber-frequency spectra were not sufficiently accurate to detect and characterize the acoustic region. Therefore applicability of source localization techniques is explored in an attempt to increase image quality and sharpness. The lack of comprehensive literature coping with physical background and limitations of beamforming algorithms inspired a ground-up step-by-step explanation including infinite and nearfield Delay-and-Sum procedures as well as the $\boldsymbol{\kappa} - \omega$ transformation and the subsequent power algorithms. The idea of deconvolution is additionally explained and derived for the different techniques. It is shown that infinite beamforming is an unbiased estimate for the $\boldsymbol{\kappa} - \omega$ transformation and as a result a non-equidistantly spaced Fourier deconvolution approach is implemented to account for spatial weighting of arbitrary microphone arrays. A range of common deconvolution procedures (DAMAS,DAMAS2,Richardson-Lucy,Lawson-Hanson) is explained and applied for infinite beamforming and the $\boldsymbol{\kappa} - \omega$ transformation to analyze their potential using a mixed Corcos-Diffuse model for the turbulent boundary layer wavenumber frequency spectrum. The Richardson-Lucy algorithm applied on a $\boldsymbol{\kappa} - \omega$ transformed map shows best results for the highly polluted acoustic region while DAMAS2 deconvolution is more efficient in removing lobes within the aerodynamic region. The deconvolution procedure is applied on experimental data at two different low machnumber cases ($M = 0.13$, $M = 0.23$). The edge of the acoustic field can for the first time be visualized for a low Machnumber case ($M = 0.23$). At $M = 0.13$ strong orthogonally impinging waves ($\boldsymbol{\kappa} = \mathbf{0}$) are detected. Isolated acoustic cross-power spectral density matrices are obtained from the deconvolved $\boldsymbol{\kappa} - \omega$-spectra by inverse Fourier transform.

Contents

NOTATION

	Mathematical Operations
$\circ$	element-wise product
$\circ/$	element-wise division
$*$	convolution
$\star$	auto-correlation
$\hat{\mathcal{F}}, \tilde{\mathcal{F}}$	Fourier transformation in time/space
$\boldsymbol{U}^H$	Hermitian transpose of $\boldsymbol{U}$

General Notation

$\boldsymbol{u}$	vector with coefficients u_i
$\boldsymbol{U}$	matrix with coefficients u_{ij}
$\hat{u}$	$\hat{\mathcal{F}}(u)$
$\tilde{u}$	$\tilde{\mathcal{F}}(\hat{u}) = \tilde{\mathcal{F}}(\hat{\mathcal{F}}(u))$
$\breve{u}$	beamformed variable u (DAS or sDAS)
$< \boldsymbol{u} >$	element-wise root mean-square of $\boldsymbol{u}$
$\lvert\boldsymbol{u}\rvert$	norm of $\boldsymbol{u}$

Domains and indexing

Γ wavenumber-frequency domain
Γ_s wavenumber-frequency source domain
Γ_f wavenumber-frequency focus domain
Ω space-frequency domain
Ω_m space-frequency domain (measurement domain)
Ω_s space-frequency source domain
Ω_f space-frequency focus domain
Θ, Ψ time/frequency domain
$\tilde{u_i} \subset \Gamma_\mathrm{s}$,$u_i \subset \Omega_\mathrm{s}$
$u_j \subset \Omega_\mathrm{m}$
$\tilde{u_l} \subset \Gamma_\mathrm{f}$,$u_l \subset \Omega_\mathrm{f}$

Variables

ω, f	angular frequency/frequency
$\boldsymbol{\kappa}, k_0$	angular wavenumber vector/ acoustic wavenumber ($k_0 = \lvert\boldsymbol{\kappa}\rvert$)
$\boldsymbol{x}, \boldsymbol{\zeta}$	absolute coordinates/ separation coordinates
$\boldsymbol{c}, c_0$	trace velocity vector/speed of sound ($c_0 = \lvert\boldsymbol{c}\rvert$))
p	pressure
q	source strength
$\underline{S}(\boldsymbol{x}, \boldsymbol{\zeta}, \omega)$	full cross-power spectral density (pressure)
$S(\boldsymbol{\zeta}, \omega)$	invariant cross-power spectral density (pressure)
$\underline{\Phi}(\boldsymbol{\kappa}, \boldsymbol{\kappa}_1, \omega)$	full wavenumber-frequency spectrum (pressure)
$\Phi(\boldsymbol{\kappa}, \omega)$	invariant wavenumber-frequency spectrum (pressure)
$\underline{\Theta}$	source cross-power spectral density (source strength)
b	beamformed map
d	deconvolved map
H	point-spread matrix
h	point-spread function
G	free-space Green function
G^i	inverse Green function

Chapter 1

Introduction

I. Wall pressure fluctuations

A broad area of engineering problems is related to the study of wall-pressure fluctuations beneath a turbulent boundary layer (TBL). An important phenomenon related to acoustics is the generation and transmission of flow induced noise causing interior noise within cars and aircraft cabins. Characterization of wall-pressure fluctuations is usually done by applying statistical methods (i.e. Cross-Covariance) on measured or simulated surface pressures. The wide range of turbulent structures evolving within the boundary layer can be described in terms of length scales or respectively wavenumbers. Wavenumber-frequency transformation allows to consider a wavenumber-frequency spectrum and hereby a more direct understanding of the underlying mechanisms. Under the assumption of homogenous turbulence one can assume that correlation lengths do not depend on the absolute measuring coordinate but only on the relative distance between two measuring points. Therefore the 4D frequency dependent cross-spectral density $S(\boldsymbol{x}, \boldsymbol{\zeta}, \omega)$ for a 2D pressure field $\hat{p}(x, y)$ can be simplified to 2D as $S(\boldsymbol{\zeta}, \omega)$. Accordingly the 4D wavenumber-frequency spectrum $\underline{\Phi}(\boldsymbol{\alpha}, \boldsymbol{\kappa}, \omega)$ becomes 2D as $\Phi(\boldsymbol{\kappa}, \omega)$. A schematic representation of $\Phi(\boldsymbol{\kappa}, \omega)$ was given by Howe [16] (Fig. 1.1a) by identifying different regions according to their respective wavenumbers. From low to high $\boldsymbol{\kappa}$ one identifies the supersonic or acoustic region enclosed by the sonic region, the subconvective region in which vortices have propagation velocities between U_∞ and c_0, the convective region (or ridge) centered around $k_c = \frac{\omega}{U_\infty}$ and the viscous region extending towards higher $\boldsymbol{\kappa}$. The sonic edge defining the acoustic contribution becomes elliptic at higher Mach-numbers (see Fig. 2.3). As the characteristic size of a vortex in direction j can be estimated as $l_j = \frac{1}{\kappa_j}$ one can directly relate the wavenumbers to their energy as originally introduced by Kolmogorov [21], thus inherently explaining the presence of a viscous region at low characterisitc lengths l. It is well prooved that the dominant region is the so-called convective ridge originating from the convective transport of turbulent structures at the mean flow velocity U_∞. Due to considerations about transmission efficiency recent research has increasingly focused on the supersonic (or acoustic) part of the spectrum.

In general the interior region is separated from the TBL by an enclosing structure (i.e. a window) whose shift invariant structural response can be described either in Ω (space-frequency domain) by $\hat{R}(\boldsymbol{\zeta}, \omega)$ or in Γ (wavenumber-frequency domain) as $\tilde{R}(\boldsymbol{\kappa}, \omega)$. The interior cross-power frequency spectrum $S^{\text{in}}(\boldsymbol{\zeta}, \omega)$ can be calculated as a spatial convolution of the frequency spectrum $S^{\text{TBL}}(\boldsymbol{\zeta}, \omega)$ with the structural response $\hat{R}(\boldsymbol{\zeta}, \omega)$. Regarding that convolution in space-frequency domain Ω can more conveniently be evaluated in Γ by simple multiplication one calculates the interior boundary wavenumber-frequency spectrum $\Phi^{\text{in}}(\boldsymbol{\kappa}, \omega)$ as

$$\Phi^{\text{in}}(\boldsymbol{\kappa}, \omega) = R(\boldsymbol{\kappa}, \omega)\Phi^{\text{TBL}}(\boldsymbol{\kappa}, \omega) \quad \text{in } \Gamma \quad \text{equivalent to} \quad S^{\text{in}}(\boldsymbol{\zeta}, \omega) = R(\boldsymbol{\zeta}, \omega) * S^{\text{TBL}}(\boldsymbol{\zeta}, \omega) \quad \text{in } \Omega \tag{1.1}$$

Maxima of structural response are found at resonant modes at which in-plane excitation velocities $U_{\text{x,y}} = \frac{\omega}{\kappa_{\text{x,y}}}$ equal mean structural wave propagation velocities U_s. Bailly et al. [1] illustrated the case by considering the bending wavenumber $k_f \sim \sqrt{\omega}$ along with estimated critical frequencies for aerodynamic $O(10Hz)$ and acoustic $O(1kHz)$ loading (Fig. 1.1b). Considerations based on a simplified analytical approach [4] or Statistical Energy

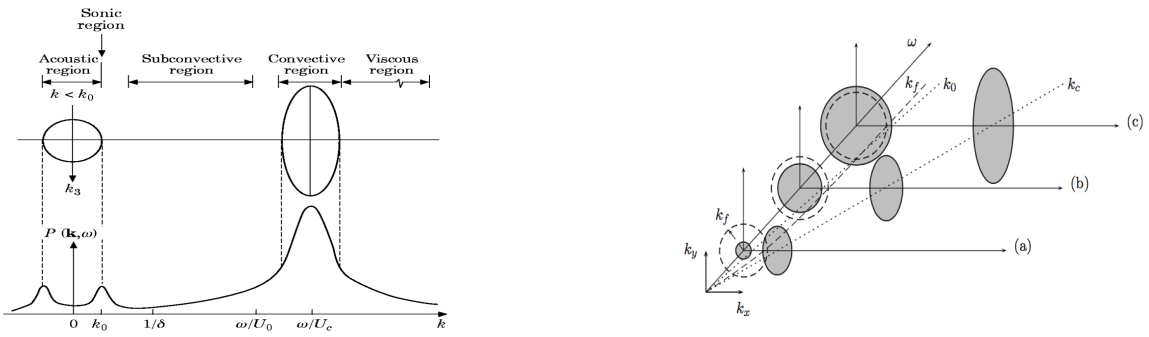

(a) $\Phi(\boldsymbol{\kappa},\omega)$ *at* $\omega = const.$ $(\omega\delta/U_\infty << 1)$*[16]*

(b) $\Phi(\boldsymbol{\kappa},\omega)$ *including bending wavenumber* k_f *[1]*

Fig. 1.1: *Modeled wavenumber-frequency spectrum*

Analysis [7] allow to estimate the transmission efficiency of a panel under acoustic load about 15 to 30 dB higher than under a turbulent pressure field. As a consequence the evaluation of properties of $\Phi(\boldsymbol{\kappa},\omega)$ in the supersonic region becomes of great importance. In case a reliable model for Φ^{TBL} could be established engineers would be able to combine acoustic ($\Phi^{\mathrm{TBL|a}}$) and aerodynamic ($\Phi^{\mathrm{TBL|d}}$) wavenumber-frequency spectra weighted with their respective transmission efficiencies ($\tilde{R}^{\mathrm{a}}$ and $\tilde{R}^{\mathrm{d}}$) to calculate the wavenumber-frequency spectrum $\Phi^{\mathrm{in}}(\boldsymbol{\kappa},\omega)$ at the interior side of the window.

$$\Phi^{\mathrm{in}}(\boldsymbol{\kappa},\omega) = \tilde{R}^{\mathrm{a}}(\boldsymbol{\kappa},\omega)\Phi^{\mathrm{TBL|a}}(\boldsymbol{\kappa},\omega) + \tilde{R}^{\mathrm{dTBL|d}}(\boldsymbol{\kappa},\omega)\Phi^{\mathrm{d}}(\boldsymbol{\kappa},\omega) \tag{1.2}$$

In general, after the evaluation of $\Phi^{\mathrm{in}}(\boldsymbol{\kappa},\omega)$ from the shift-invariant cross-power spectrum $S(\boldsymbol{\zeta},\omega)$, spectral application of Parsevals theorem yields the resulting transmitted acoustic mean square pressure $\langle\hat{p}^{\mathrm{in|a}}\rangle$ corresponding to $S(\mathbf{0},\omega) = \langle\hat{p}^{\mathrm{in|a}}\rangle^2$ as

$$\langle\hat{p}^{\mathrm{in|a}}\rangle^2 = \int_{\boldsymbol{\kappa}\in\Gamma} \Phi^{\mathrm{in}}(\boldsymbol{\kappa},\omega)\boldsymbol{d}\kappa \tag{1.3}$$

Describing the characteristics of TBL noise in dependence of a specific window response is rather unpractical. The TBL is therefore itself described by a superposition of acoustic and hydrodynamic contribution $\langle\hat{p}^{\mathrm{TBL}}\rangle^2 = \langle\hat{p}^{\mathrm{TBL|a}}\rangle^2 + \langle\hat{p}^{\mathrm{TBL|d}}\rangle^2$ with the individual contributions being evaluable from $\Phi^{TBL}(\boldsymbol{\kappa},\omega)$ by integrating over aerodynamic (Γ_{a}) and acoustic (Γ_{d}) domain yielding respectively

$$\langle\hat{p}^{\mathrm{TBL|a}}\rangle^2 = \int_{\boldsymbol{\kappa}\in\Gamma_{\mathrm{a}}} \Phi(\boldsymbol{\kappa},\omega)\boldsymbol{d}\kappa \quad \text{and} \quad \langle\hat{p}^{\mathrm{TBL|d}}\rangle^2 = \int_{\boldsymbol{\kappa}\in\Gamma_{\mathrm{d}}} \Phi(\boldsymbol{\kappa},\omega)\boldsymbol{d}\kappa \tag{1.4}$$

The wide range of wavenumbers covered by hydrodynamic and acoustic region makes measurement of Φ^{TBL} a challenging task. Diverse approaches have been developed to accomplish this task in recent studies.

1. Direct spatial Fourier transform

   An equidistant transducer array is used to be able to directly apply the FFT algorithm on the resulting cross-power frequency spectrum. This implies a huge number of sensor in case direct acoustic sound shall be measured. To avoid aliasing the spatial sampling rate has to be at least $\kappa_{\mathrm{samp}} \geq 2\kappa_{\mathrm{c}}$ resulting in a transducer distance of $l_{\mathrm{dis}} = \frac{2\pi}{\kappa_{\mathrm{c}}}$ while a sufficient resolution of the acoustic region requires a large measuring distance according to $\Delta\kappa = \frac{2\pi}{l_{\mathrm{array}}}$. These opposing requirements result in a huge amount of microphones and thus only few studies use this approach.

2. Analysis of the vibratory response

   Another approach is based on the analysis of the vibratory response of the excited structure. By using small plates with known vibratory responses it is possible to measure the wavenumbers associated to each vibration mode. A main disadvantage of this technique is that only few wavenumbers are available.

3. Non-equidistant transducer arrays

   A promising technique is to overcome the restrictions posed by the FFT by using non-equidistant transducer arrays. The resulting spectrum can be obtained by using plane-wave beamforming or a non-equidistant Fourier transform. Capabilities of the non-equidistant Fourier transform are difficult to access but this backdraw can be compensated for by evaluating the post-processing with analytial models. The following two example of measurements are based on this technique followed by deconvolution procedures to enhance the quality of the resulting spectrum.

Ehrenfried et al. [11] performed wavenuber-frequency spectrum measurements by using the experimental setup sketched in Fig. 1.2a with the transducer position shown in Fig. 1.2b for a high Mach number flow ($M = 0.83$). The resulting spectrum Fig. 1.2c obtained by infinite beamforming and DAMAS2 deconvolution suggests the presence of acoustic waves within the acoustic domain but the expected sonic ridge could not be visualized. The reason for these results remains unclear.

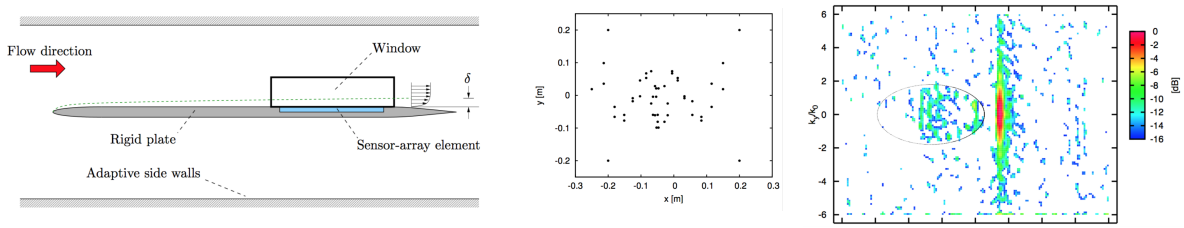

(a) *Setup* **(b)** *Transducer array* **(c)** *Measured $\kappa - \omega$ spectrum*

Fig. 1.2: *Experimental case Ehrenfried [11]*

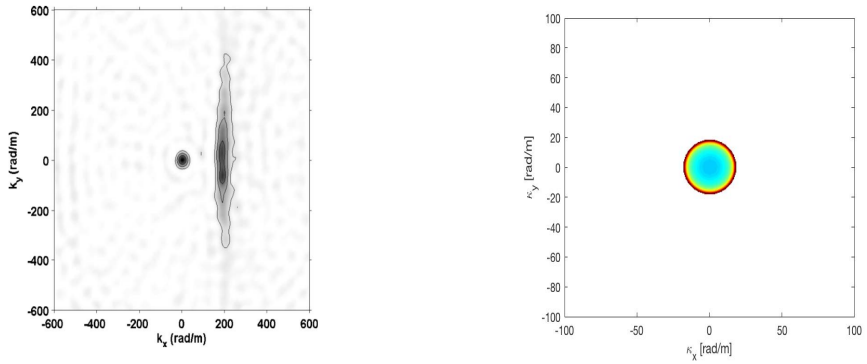

(a) $\Phi(\boldsymbol{\kappa}, \omega)$ *at* $f = 1000Hz$ *[1]* **(b)** *Diffuse field model* $\Phi^{\mathrm{a}}(\boldsymbol{\kappa}, \omega)$

Fig. 1.3: *Measurement of Bailly et. al [1] and Diffuse field model*

II. Previous experimental research

Basis of this work is measured data published by Bailly et al. [1] (see Fig. 1.3a) using a non-equidistant microphone array. Results show convenient resolution of the convective region but the acoustic region expected to be characterized by the sonic edge shown in Fig. 1.3b remains masked by the microphone response. The presence of strong orthogonally impinging waves seems to hide the expected diffuse field, best localizable through the sonic region appearing as a high amplitude circle at the acoustic wavenumber $\kappa_0 = \frac{\omega}{c_0}$ (see Fig. 1.3b). Removing the microphone response in a deconvolution approach seems promising to reveal further details about the nature of the measured low wavenumber region. It is expected that the deconvolved image shows a single high amplitude

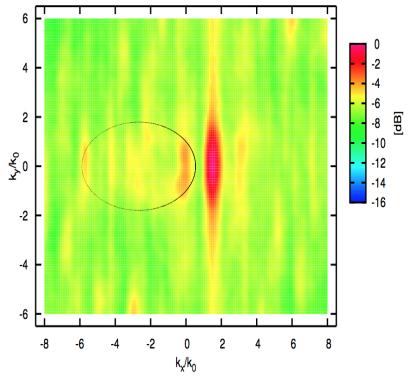

(a) *Dirty map* $\check{\Phi}(\boldsymbol{\kappa}, \omega)$ *at* $f = 1758Hz$ $(M = 0.83)$ *[10]*

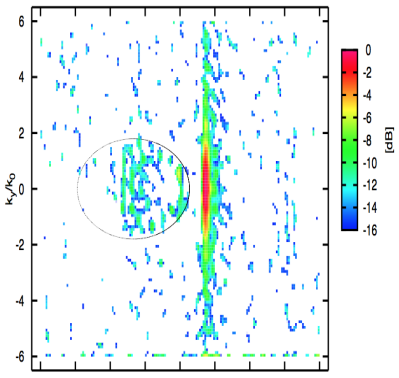

(b) *Deconvolved map* $\tilde{\Phi}(\boldsymbol{\kappa}, \omega)$ *at* $f = 1758Hz$ $(M = 0.83)$

Fig. 1.4: *Maps obtained by Ehrenfried et al. [10]*

point at $\boldsymbol{\kappa} = \mathbf{0}$ as well as a strong concentration of energy around the acoustic circle. Such a devonvolution approach was applied by Ehrenfried [11] to postprocess a high Mach number ($M = 0.83$) TBL experiment. A plane wave beamforming algorithm was used to evaluate the dirty map Fig. 1.4a followed by a DAMAS2 deconvolution procedure to estimate the underlying source map Fig. 1.4b. Sidelobes were efficiently supressed revealing structures within the acoustic domain. Unexpectedly these structures are not aligned on the sonic circle but distributed more densely around $\boldsymbol{\kappa} = \mathbf{0}$. An explanation for these results is still lacking.

III. Convolution & Deconvolution on a simple example

Deconvolution (also known as Deblurring) is a signal processing method widely used in image processing. It is applicable to images whose real structure is blurred due to recording errors of imperfect recording devices. Fig. 1.5a shows a close-up chessboard image being blurred due to the cameras limited focusing range. The camera response is shown in Fig. 1.5b.

The point-spread function can be evaluated analytically if the reason for blurring is known and can be described physically (optics: lense, acoustics: finite microphone array). In case of unknown blurring reason one can use blind-deconvolution algorithms that guess the PSF based on maximum-likelyhood methods.

As the blurred image b is related through convolution to the deblurred image d as $b = h *_{\mathrm{v,i}} d$ (where $*_{\mathrm{v,i}}$ denotes shift-variant or invariant convolution and h the PSF) one can use a range of algorithms to solve the discrete problem ($\boldsymbol{b} = \boldsymbol{H}\boldsymbol{d}$). Application of the Richardson-Lucy algorithm on Fig. 1.5a with point-spread function Fig. 1.5b gives 1.5c.

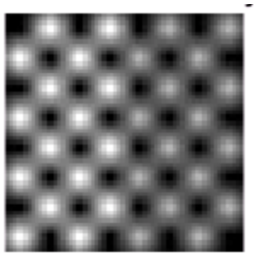

(a) *close-up Chessboard*

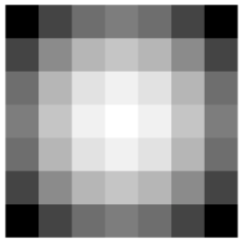

(b) *optical PSF*

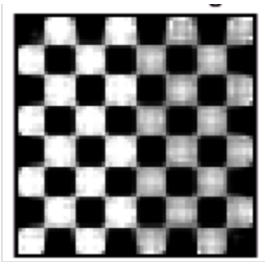

(c) *deblurred Image*

Fig. 1.5: *Deblurring example*

Chapter 2

Signal processing

Deconvolution of wavenumber-frequency spectra is an advanced signal processing procedure based on a range of mathematical concepts, including especially the principle of convolution and the Fourier transform. For a comprehensible introduction into these subjects [22] is recommended. The application of deconvolution within the acoustic community has strongly increased since the introduction of DAMAS in 2005 by Brooks & Humphreys [5] and the ensuing development of DAMAS2 by Dougherty [8]. Nevertheless comprehensive literature covering the application of deconvolution in acoustics is still lacking. Therefore an attempt is made to provide ground-up derivations of infinite Delay-and-Sum (iDAS), near-field (or spherical) Delay-and-Sum (sDAS) and the generalized discrete Fourier transform ($\boldsymbol{\kappa} - \omega$ transformation) along with their respective power-algorithns in order to provide access to relevant scientific articles covering deconvolution attempts to each of them. The theoretic part starts with a short introduction into signal processing basics and statistics, followed by an overview over the wave equation and its solutions, subsequent derivations of amplitude and power algorithms for $\boldsymbol{\kappa} - \omega$ transformation, DAS, sDAS along with their respective point-spread functions and ends by a presentation of a range of common deconvolution procedures.

I. Basics

a. Convolution

Convolution is a powerful mathematical operation evolving from the definition of the scalar product. A convolution of a function $g(t)$ with a function $h(t)$ can be interpreted as the projection from $g(t)$ on the flipped $h(t)$ over Θ with upper bound t. Function $h(t)$ can be referred to as the convolution kernel.

$$r(t) = (g * h)(t) = \int_{\partial\Theta} g(t')h(t - t')dt' \tag{2.1}$$

b. Discrete Convolution

In signal and image processing convolution is most frequently applied on discrete functions. Thus a discrete convolution can be defined by replacing the integral by a sum. If $g, h : D \to \Theta$ are functions with discrete definition area $D \subseteq \Theta$ the discrete convolution is defined as:

$$(f \overline{*} g)(n) = \sum_{k \in D} f(k)g(n - k) \tag{2.2}$$

c. Convolution and discrete Convolution

Calculating the convolution $f * g$ in a discrete way is not the same as calculating the discrete convolution $g \overline{*} h$.

$$f * g \approx \sum_{k \in D} f(t_k) g(t_n - t_k) \Delta t_k \quad \text{whereas} \quad \mathrm{f} \bar{*} \mathrm{g} \approx \sum_{\mathrm{k} \in \mathrm{D}} \mathrm{f}(\mathrm{t_k}) \mathrm{g}(\mathrm{t_n} - \mathrm{t_k}) \tag{2.3}$$

Convolution represents a temporal average over Θ whereas discrete convolution is just a discrete (unbiased) estimate over function values belonging to subspace D. This will be of particular importance when dealing with nonequidistant sampling.

d. Cross-Correlation

The correlation is defined similar to convolution with the only difference that the convolution $r(t) = (g * h)(t)$ reflects the integration over the product of $g(t)$ with a shifted reversed (up-down flipped) function $h(t)$ while correlation reflects the integrated product with a shifted only function.

$$r(t) = g(t) \star h(t) = \int_{-\infty}^{\infty} g(t') h(t + t') dt' \tag{2.4}$$

Note that the terminus cross-correlation applied in the sense $\boldsymbol{r} = \boldsymbol{g} \star \boldsymbol{h}$ denotes the vector $\boldsymbol{r}$ resulting from the convolution of $\boldsymbol{g}$ with the reversed vector of $\boldsymbol{h}$.

e. The Fourier transform

The Fourier transform is a powerful tool used in a wide range of engineering areas. One among many other applications is the possibility to analyze and process time-dependent signals in frequency domain or, as explored in this work, space-time dependent signals in wavenumber-frequency domain. Linear operations in one domain have corresponding operations in the other domain. If $\Theta \in \mathbb{R}$ denotes the time domain with frequency domain $\Psi \in \mathbb{C}$ then Ψ represents a complete orthogonal system with complex exponential bases $e^{i\omega t}$, where ω denotes the angular frequency given in $[\frac{rad}{s}]$ related to the temporal frequency f in Hertz $[Hz]$ by $\omega = 2\pi f$. The different representations are frequently referred to as a Fourier transform pair. Time and frequency representation are related the following:

$$\hat{g}(\omega) = \frac{1}{2\pi} \int_{\partial\Theta} g(t) e^{-i\omega t} dt = \hat{\mathcal{F}} g(t) \tag{2.5}$$

and

$$g(t) = \int_{\partial\Psi} \hat{g}(\omega) e^{i\omega t} dt = \hat{\mathcal{F}}^{-1} \hat{g}(\omega) \tag{2.6}$$

The Fourier transform exchanges convolution operations with multiplications. Given two integrable functions $g(t)$ and $h(t)$ with Fourier transforms $\hat{g}(\omega)$ and $\hat{h}(\omega)$ then the Fourier transformation of the temporal convolution of $g(t)$ and $h(t)$ equals the product of $\hat{g}(\omega)$ and $\hat{h}(\omega)$.

$$r(t) = g(t) * h(t) \quad \Longleftrightarrow \quad \hat{r}(\omega) = g(\omega) h(\omega) \tag{2.7}$$

f. The wavenumber-frequency transformation

The wavenumber-frequency transformation can beneficially be used to analyze wave fields. It will be one of the main topics in this work and explained in detail later on. The notation in use is:

$$\tilde{p}(\boldsymbol{\kappa}, \omega) = \tilde{\mathcal{F}} \hat{\mathcal{F}} p(\boldsymbol{x}, t) = \frac{1}{(2\pi)^d} \int_{\partial\Omega} \frac{1}{2\pi} \int_{\partial\Theta} p(\boldsymbol{x}, t) e^{-i\omega t} dt e^{-i\boldsymbol{\kappa}\boldsymbol{x}} d\boldsymbol{x} \tag{2.8}$$

g. The cross-power spectral density S

The cross-power spectral density or (cross-power spectrum) is a powerful tool to analyze the spatial coherence of temporally Fourier transformed signals. It can be defined as the temporal Fourier transform of spatial covariance data measured over time. For an acoustic array with measured pressures $p(\boldsymbol{x}, \boldsymbol{t})$ it reads:

$$\underline{S}(\boldsymbol{x}, \boldsymbol{\zeta}, \omega) = \lim_{T \to \infty} \frac{2\pi}{T} E\left[\hat{p}(\boldsymbol{x}, \omega) \hat{p}^*(\boldsymbol{x} + \boldsymbol{\zeta}, \omega)\right] \tag{2.9}$$

where $\boldsymbol{\zeta}$ is a vector with components (ζ, η) that correspond to the (cartesian) separation distance between the n_{M} microphones in x and y direction. $E[]$ denotes the ensemble averaging over a sufficiently high number of statistically independent measurements and $\hat{p}^*$ is the conjugate of $\hat{p}$. It is important to note that the cross-power spectral density resulting from 1D data contains 2-D spatial covariance information and respectively for higher dimensions. Physical interpretation of $\underline{S}(\boldsymbol{x}, \boldsymbol{\zeta}, \omega)$ can in detail be found in [23]. By looking at the covariance spectrum for a given absolute coordinate $\boldsymbol{x}$ and a given frequency ω one can detect phase shifts characterized by high correlation for correlation length displacements $\boldsymbol{\zeta}$ towards a specified direction.

$\underline{S}(\boldsymbol{x}, \boldsymbol{\zeta}, \omega)$ can be simplified as $S(\boldsymbol{\zeta}, \omega)$ in the case of shift invariance. Shift-invariance can be assumed if the correlation between a measurement at $\boldsymbol{x}$ and $\boldsymbol{x} + \boldsymbol{\zeta}$ depends not on the absolute position $\boldsymbol{x}$ but is only a function of the relative distance between two measurements $\boldsymbol{\zeta}$. This is exactly the case only for plane wave fields. Note also that assuming shift-invariance does not allow analyzation of coherence characteristics.

In case of shift-invariance $S(\mathbf{0}, \omega)$ equals the squared mean pressure $\langle \hat{p} \rangle^2$.

$$\langle \hat{p} \rangle^2(\boldsymbol{x}, \omega) = \underline{S}(\boldsymbol{x}, \mathbf{0}, \omega) \Rightarrow \langle \hat{p} \rangle^2(\omega) = S(\mathbf{0}, \omega) \tag{2.10}$$

In case of shift-invarance $\langle \hat{p} \rangle^2(\omega)$ does not depend on $\boldsymbol{x}$ as postulated by the plane wave assumption.

h. The wavenumber-frequency spectrum

The full wavenumber frequency spectrum (or wavenumber frequency covariance spectrum) $\underline{\tilde{\Phi}}(\boldsymbol{\kappa}_{\mathrm{x}_1}, \boldsymbol{\kappa}_{\mathrm{x}_2}, \omega)$ can be defined as the 4D spatial Fourier transform of $\underline{S}(\boldsymbol{x}, \boldsymbol{\zeta}, \omega)$:

$$\underline{\tilde{\Phi}}(\boldsymbol{\kappa}_1, \boldsymbol{\kappa}_2, \omega) = \tilde{\mathcal{F}}^{4\mathrm{D}} \underline{S}(\boldsymbol{x}, \boldsymbol{\zeta}, \omega) \tag{2.11}$$

Similar to $\underline{S}$ one can use $\underline{\tilde{\Phi}}(\boldsymbol{\kappa}_{\mathrm{x}_1}, \boldsymbol{\kappa}_{\mathrm{x}_2}, \omega)$ to analyze coherence of wave fields. For a given wavenumber κ_1 one can interpret high values over displacement wavenumber κ_2 as wavenumber domain correlation length displacements (thus phase shifts).

Under the assumption of shift-invariance, the reduced wavenumber frequency spectrum can be defined as the 2D spatial Fourier transform of $\boldsymbol{S}(\boldsymbol{\zeta}, \omega)$.

$$\tilde{\Phi}(\boldsymbol{\kappa}, \omega) = \tilde{\mathcal{F}}^{2\mathrm{D}} \boldsymbol{S}(\boldsymbol{\zeta}, \omega) \tag{2.12}$$

In plane wave acoustic source localization (infinite beamforming)a discrete convolution is performed opposing the spatial convolution resulting in the Fourier transform.The resulting dirty map can be considered a wavenumber-frequency-like spectrum and is thus denoted $\breve{\phi}(\boldsymbol{\kappa}, \omega)$. It will be explained in more detail in III.

i. Parsevals theorem

Parseval's theorem reflects energy conservation during the Fourier transformation. For shift-invariant transformation from spatial domain $\partial\Omega$ to wavenumber domain $\partial\Gamma$ one can write it as:

$$\int_{\partial\Omega} |\hat{p}(\boldsymbol{\zeta}, \omega)|^2 d\boldsymbol{\zeta} = \frac{1}{(2\pi)^d} \int_{\partial\Gamma} |\tilde{p}(\boldsymbol{\kappa}, \omega)|^2 d\boldsymbol{\kappa} \tag{2.13}$$

By mentioning that $\int_{\partial\Omega} |\hat{p}(\boldsymbol{\zeta}, \omega)|^2 d\boldsymbol{\zeta}$ is the auto-power $\langle \hat{p} \rangle^2(\boldsymbol{x}, \omega) = S(\mathbf{0}, \omega)$ and $|\tilde{p}(\boldsymbol{\kappa}, \omega)|^2$ is the shift-invariant wavenumber-frequency spectrum $\Phi(\boldsymbol{\kappa}, \omega)$ one can rewrite (2.13):

$$S(\mathbf{0},\omega) = \frac{1}{(2\pi)^d}\int_{\partial\Gamma}\Phi(\boldsymbol{\kappa},\omega)\boldsymbol{d}\kappa \tag{2.14}$$

II. The Wave equation

a. Definition

Following [18] one can derive Lighthill's equation by combining the temporal derivation of mass conversation with the spatial derivative on the Reynolds form of the momentum equation for an ideal, linear acoustic medium forced by an external stress distribution $-\frac{\partial L_{ij}}{\partial x_j}$ resulting from the real fluid. The speed of sound is denoted c_0 and p' is the deviation from the spatial mean pressure. Influence of mean flow on the speed of sound can be neglected for low Mach number flows. The resulting equation becomes :

$$\frac{1}{c_0^2}\frac{\partial^2 p'}{\partial t^2} - \frac{\partial^2 p'}{\partial x_i^2} = \frac{\partial^2 L_{ij}}{\partial x_i \partial x_j} \tag{2.15}$$

For low Mach numbers the Lightill tensor L_{ij} can be estimated as :

$$L_{ij} = \frac{\partial^2 \rho_0 (u_i u_j - \overline{u_i u_j})}{\partial x_i \partial x_j} \tag{2.16}$$

where $\overline{u_i u_j}$ is the ensemble averaged spatial mean.

The homogenous problem ($L_{ij} = 0$) is the well-known wave equation. As every solution of the Lighthill equation is also a solution of the wave equation it will be used to explain possible solutions and their physical interpretation. For simplicity p' will furthermore simply be denoted by p.

$$\frac{1}{c_0^2}\frac{\partial^2 p}{\partial t^2} - \nabla^2 p = 0 \tag{2.17}$$

Its temporal Fourier transform , also known as Helmholtz equation, becomes (using $\tilde{\mathcal{F}}(\frac{\partial p(t)}{\partial t}) = -i\omega\hat{p}(\omega)$)

$$\nabla^2 \hat{p} + k_0^2 \hat{p} = 0 \tag{2.18}$$

with the acoustic wavenumber $\kappa_0 = \frac{\omega}{c_0}$. For convenience we define the velocity vector $\boldsymbol{c} = [c_\mathrm{x}, c_\mathrm{y}, c_\mathrm{z}]$ where $c_\mathrm{x}, c_\mathrm{y}, c_\mathrm{z}$ are the trace velocites in each axis. Correspondingly component κ_l of trace wavenumber vector $\boldsymbol{\kappa}$ is defined as $\kappa_l = \frac{\omega}{c_l}$. Note that $|\boldsymbol{c}| = c_0$ and $|\boldsymbol{\kappa}| = \kappa_0$.

b. Plane, spherical and evanescent waves

Every solution of (2.18) has the following shape:

$$\hat{p}(\boldsymbol{x},\omega) = \hat{A}(\omega)e^{i(\kappa_\mathrm{x}x+\kappa_\mathrm{y}y+\kappa_\mathrm{z}z)} \quad \boldsymbol{x}\in\mathbb{R}^3 \tag{2.19}$$

where $A(\omega)$ is a frequency dependent constant. (2.19) satisfies (2.18) as long as the dispersion relation is satisfied

$$\kappa_0^2 = \kappa_\mathrm{x}^2 + \kappa_\mathrm{y}^2 + \kappa_\mathrm{z}^2 \tag{2.20}$$

Fig. 2.1 shows a plane wave with frequency ω impinging under angle θ where $\theta = 0$ represents a wave travelling in positive x-direction and $\theta = \frac{\pi}{2}$ a wave travelling in positive z-direction orthogonal to the x-y-plane. If the wave propagates within the x-y plane, $\kappa_\mathrm{z} = 0$, the κ-space representation shows a point on the circle with radius=κ. If θ is increasing, meaning the wave is travelling towards z-direction, the white stripes representing the wave traces are turning from vertical (x-y plane wave) to horizontal lines. Therefore the wavelengths λ_x and λ_y

are increasing and the corresponding wavenumbers $\kappa_x = \frac{2\pi}{\lambda_x}$,$\kappa_y = \frac{2\pi}{\lambda_y}$ are reduced, causing the point in the κ-space representation to move inwards. At $\theta = \frac{\pi}{2}$ the wave impinges orthogonally to the $x-y$-plane, reflecting in an infinite wavelength λ_x,λ_y. As $\kappa_x = \frac{\omega}{c_x}$ the trace velocity $c_x \to \infty$ and the x-y wavenumber representation becomes a point at the origin of the coordinate system.

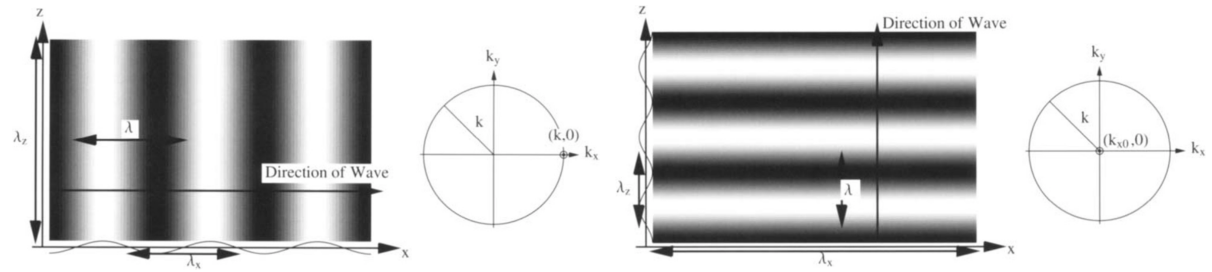

Fig. 2.1: *Plane wave representation examples [9]*

Equation (2.20) still satisfies the wave equation if κ_x or $\kappa_y > \kappa_0$, which turns the plane waves into evanescent waves. The wavenumber component in z-direction can then be written as

$$\kappa_z = \pm i\sqrt{\kappa_x^2 + \kappa_y^2 - k^2} = \pm i\kappa_z' \tag{2.21}$$

with the plane wave solution

$$\hat{p}(\boldsymbol{x}, \omega) = \hat{A}(\omega) e^{\pm \kappa_z' z} e^{i(\kappa_x x + \kappa_y y)} \tag{2.22}$$

The $e^{+\kappa_{z'} z}$ solution is unphysical since it blows up at positive infinity. Thus the only possible solution becomes:

$$\hat{p}(\boldsymbol{x}, \omega) = \hat{A}(\omega) e^{-\kappa_z' z} e^{i(\kappa_x x + \kappa_y y)} \tag{2.23}$$

The evanescent wave is decaying exponentially in amplitude in the z-direction. Since $\kappa_x > \kappa_0$, one has $c_x < c_0$ and thus the trace velocity is subsonic. Evanescent waves are therefore called subsonic waves, having their wavenumber representation always outside the radiation circle as shown in Fig. 2.2

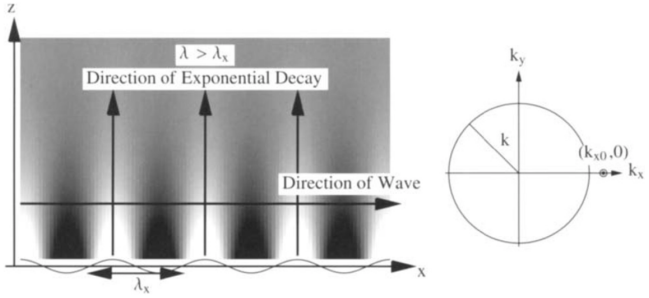

Fig. 2.2: *Evanescent wave representation example [9]*

c. Wavespace representation

It has already been shown that the dispersion relation is fulfilled for every solution of the wave equation. Through (2.21) every solution in $\mathbb{R}^3$ can be obtained from $\mathbb{R}^2$.It is therefore sufficient to define the 2D solution as:

$$\hat{p}(\boldsymbol{x}, \omega) = \hat{A}(\omega) e^{i\boldsymbol{\kappa}_s \boldsymbol{x}} \quad \text{for} \quad \boldsymbol{x}, \boldsymbol{\kappa}_s \in \mathbb{R}^2 \tag{2.24}$$

Displaying planar solutions of the Helmholtz equation as points in wavenumber-frequency space already suggests the idea of spatially Fourier transforming $\hat{p}(\boldsymbol{x}, \omega)$ to obtain the plane wave fundamental solution as:

$$\tilde{p}(\omega, \boldsymbol{\kappa}) = \tilde{\mathcal{F}} e^{i\boldsymbol{\kappa}_\mathrm{s}\boldsymbol{x}} = \delta(\boldsymbol{\kappa} - \boldsymbol{\kappa}_\mathrm{s}) \tag{2.25}$$

Note that this does not mean that all representations of data in wavenumber-frequency domain are to be considered as solutions of the wave equation. But if they can be assumed as plane waves then the full field in $\mathbb{R}^3$ can be completely restored from data in $\mathbb{R}^2$. This forms the basics of Fourier Acoustics [9]. In case of higher Mach-numbers $M >> 0$ the mean flow velocity has to be taken into account through a convected plane-wave propagator. The dispersion relation becomes elliptically stretched in mean flow direction.

d. Spherical waves

The elementary plane wave (2.19) is not the only solution of the wave equation. It can be shown that

$$G(\boldsymbol{x} - \boldsymbol{x}_\mathrm{s}) = \frac{e^{-i\omega\frac{|\boldsymbol{x}-\boldsymbol{x}_\mathrm{s}|}{c_0}}}{|\boldsymbol{x} - \boldsymbol{x}_\mathrm{s}|} = \frac{e^{-i\kappa_0|\boldsymbol{x}-\boldsymbol{x}_\mathrm{s}|}}{|\boldsymbol{x} - \boldsymbol{x}_\mathrm{s}|} \tag{2.26}$$

is also a solution of the Helmholtz equation. It corresponds to a spherically symmetric unit strength point source with wavenumber κ_0 at spatial position $\boldsymbol{x}_\mathrm{s}$ and is generally referred to as free-space Green's function. According to distribution theory it is possible to calculate the solution for an arbitrary source field $\hat{q}_\mathrm{s}(\boldsymbol{x}_\mathrm{s}, \omega)$ with $\boldsymbol{x}_\mathrm{s} \in \Omega_\mathrm{s}$ by convolving the source distribution with the fundamental solution (or convolution kernel) $G(\boldsymbol{x}_\mathrm{s}, \omega)$ as

$$\hat{p}(\boldsymbol{x}, \omega) = \hat{q}_\mathrm{s}(\boldsymbol{x}_\mathrm{s}, \omega) \overline{*} G(\boldsymbol{x}_\mathrm{s}, \omega) = \sum_{\boldsymbol{x}_\mathrm{s} \in \Omega_\mathrm{s}} \hat{q}(\boldsymbol{x}_\mathrm{s}, \omega) \frac{e^{-i\kappa_0|\boldsymbol{x}-\boldsymbol{x}_\mathrm{s}|}}{|\boldsymbol{x} - \boldsymbol{x}_\mathrm{s}|} \tag{2.27}$$

e. Acoustic domain under the presence of a mean flow

Under the presence of a mean flow with Mach number M the sonic wavenumbers are those that fulfill the convective dispersion relation$(k_0 - k_\mathrm{x}M)^2 - (k_x^2 + k_y^2) = 0$. Introducing the Prandtl-Glauert parameter $\beta = \sqrt{1 - M^2}$ one can represent the dispersion relation as the ellipse fulfilling the following equation:

$$\frac{(k_\mathrm{x} + \frac{k_0 M}{\beta^2})^2}{(\frac{k_0}{\beta^2})^2} + \frac{k_\mathrm{y}^2}{(\frac{k_0}{\beta^2})^2} = 1 \tag{2.28}$$

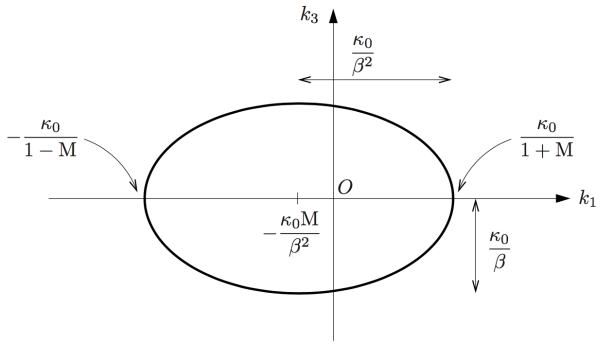

Fig. 2.3: *Acoustic domain under the presence of a mean flow with Mach number M [14]*

Supersonic (or acoustic) waves are located inside the ellipse while subsonic (or hydrodynamic) evanescent waves are located outside.

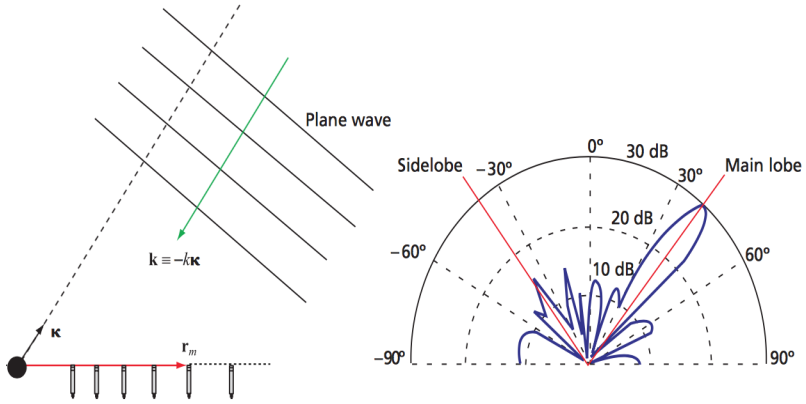

Fig. 2.4: *A microphone array with plane wave impinging under wavevector $\boldsymbol{\kappa}$ and its directional sensitivity diagramm [17]*

f. Propagation models

As already mentioned (2.19) and (2.23) are solutions of the Helmholtz equation. These equations reflect the physical behavior of waves. The choice of a suitable model depends on assumptions about the nature of the observed field.

Three different propagator models are in use for a single unity strength source at position $\boldsymbol{x}_\mathrm{s} \in \Omega_\mathrm{s}$ (for spherical waves) with wavenumber $\boldsymbol{\kappa}_\mathrm{s} \in \Gamma_\mathrm{s}$.

1. The infinite propagator for plane waves: $\tilde{p}(\boldsymbol{\kappa}_\mathrm{s}, \omega) = \tilde{\mathcal{F}}\hat{p}(\boldsymbol{x}, \omega) = \delta(\boldsymbol{\kappa} - \boldsymbol{\kappa}_\mathrm{s})$
2. The farfield propagator : $\hat{p}(\boldsymbol{x}, \omega) = \frac{e^{-i\kappa_0|\boldsymbol{x}-\boldsymbol{x}_\mathrm{s}|}}{z}$ for spherical waves with planar wavefront originating from farfield sources for which assumption $|\boldsymbol{x} - \boldsymbol{x}_\mathrm{s}| \approx z$ holds
3. The neafield propagator : $\hat{p}(\boldsymbol{x}, \omega) = G(\boldsymbol{x} - \boldsymbol{x}_\mathrm{s}, \omega) = \frac{e^{-i\kappa_0|\boldsymbol{x}-\boldsymbol{x}_\mathrm{s}|}}{|\boldsymbol{x}-\boldsymbol{x}_\mathrm{s}|}$ for spherical waves

III. Infinite DAS and the $\kappa - \omega$ transformation

Delay-and-Sum is a signal processing technique being widely used for acoustic source detection as well as directional signal transmission. A sensor array records incoming signals. The measured signals are individually backpropagated and summed to match an assumed source position using an appropriate propagator model. In case the backpropagated signal matches the real one constructive interference leads to a peak in the so-called dirty map. The following abbreviations will be used:

- iDAS the infinite Delay-and-Sum
- sDAS for nearfield (spherical) Delay-and-Sum

a. Infinite Delay-and-Sum (iDAS)

Figure 2.4 explains the basic idea of iDAS. Considering a planar array of N microphones at locations $\boldsymbol{x}_m (m = 1, 2, ..., N)$ in the xy-plane. Applying the DAS algorithm means that the measured pressure signals $\hat{p}_m$ are individually delayed in time to match an assumed incidence direction characterized by wavenumber vector $\boldsymbol{\kappa}$ and then summed. Additionally each $\hat{p}_m$ is multiplied with an arbitrary weighting coefficient w_m for which $\sum_{j=1}^{N} w_j = N$ holds. Beamformer with non-unity weights are called functional beamformers. Signals associated with a plane wave coming from $\boldsymbol{\kappa}$ will therefore be aligned in time before they are summed. The result is weighted with $\frac{1}{N}$ to obtain the correct amplitude of a single impinging wave. For convenience discrete subsets are defined as $\boldsymbol{x} \in \Omega_\mathrm{d} \subseteq \Omega$ and $t \in \Theta_\mathrm{d} \subseteq \Theta$. N is the number of values in subset Ω_d. The iDAS algorithm reads:

$$\breve{p}(\boldsymbol{\kappa}, t) = \frac{1}{N} \sum_{\boldsymbol{x} \in \Omega_\mathrm{d}} w(\boldsymbol{x}) p(\boldsymbol{x}, t - \Delta t(\boldsymbol{\kappa}, \boldsymbol{x})) \quad \text{with} \quad \Delta t = \frac{\boldsymbol{\kappa x}}{\omega} \tag{2.29}$$

In practice (2.29) is computationally inefficient because it cannot be vectorized. Thus temporal Fourier transformation is applied on $p(\boldsymbol{x}, t + \Delta t(\boldsymbol{\kappa}, \boldsymbol{x}))$ yielding:

$$\hat{\mathcal{F}} p(\boldsymbol{x}, t - \Delta t(\boldsymbol{\kappa}, \boldsymbol{x})) = \hat{p}(\boldsymbol{x}, \omega) e^{-i\omega \Delta t(\boldsymbol{\kappa}, \boldsymbol{x})} = \hat{p}(\boldsymbol{x}, \omega) e^{-i\boldsymbol{\kappa x}} \tag{2.30}$$

Therefore the infinite DAS algorithm in frequency notation becomes:

$$\breve{p}(\boldsymbol{\kappa}, \omega) = \frac{1}{N} \sum_{\boldsymbol{x} \in \Omega_\mathrm{d}} w(\boldsymbol{x}) \hat{p}(\boldsymbol{x}, \omega) e^{-i\boldsymbol{\kappa x}} \tag{2.31}$$

b. Infinite DAS and the wavenumber-frequency transformation

Both iDAS and the $\boldsymbol{\kappa} - \omega$ transformation ($\tilde{p} = \tilde{\mathcal{F}} \hat{\mathcal{F}} \hat{p}$) yield maps in wavenumber-frequency space. The relation between the two is often misunderstood and cannot be found in literature. The effect becomes clear when looking at their discrete counterparts:

$$\tilde{p}(\boldsymbol{\kappa}, \omega) = \frac{1}{(2\pi)^d} \sum_{\boldsymbol{x} \in \Omega_\mathrm{d}} \hat{p}(\boldsymbol{x}, \omega) e^{-i\boldsymbol{\kappa x}} \Delta \boldsymbol{x} \quad \text{vs} \quad \breve{p}(\boldsymbol{\kappa}, \omega) = \frac{1}{N} \sum_{\boldsymbol{x} \in \Omega_\mathrm{d}} w(\boldsymbol{x}) \hat{p}(\boldsymbol{x}, \omega) e^{-i\boldsymbol{\kappa x}} \tag{2.32}$$

In case of equidistant array structure $\Delta \boldsymbol{x}$ (denoting the affiliated microphone areas corresponding to position $\boldsymbol{x}$ is constant and in case of unity weights $w(x)$ the DAS map $\breve{p}(\boldsymbol{\kappa}, \omega)$ becomes just a scaled version of $\tilde{p}(\boldsymbol{\kappa}, \omega)$.

Literature about the discrete Fourier transform generally considers the temporal transformation in frequency domain given frequency f or angular frequency ω where $\omega = 2\pi f$ holds. Note that the corresponding variables for the spatial transformation become wavenumber k or angular wavenumber κ for which $\kappa = 2\pi k$ holds equally.

An equidistant array with length L and N measuring microphones is assumed. The discrete Fourier transformation is an orthogonal projection, thus N κ-space bases can be projected on. According to the sampling theorem the κ-space resolution becomes $\Delta\kappa = 2\pi\Delta k = 2\pi\frac{1}{L} = 2\pi\frac{1}{N\Delta x}$.

The discrete spatial Fourier transform translates pressures $\hat{p}_n(\boldsymbol{x}, \omega)$ with $n \in [1; N]$ from discrete spatial coordinates x_j

$$x_j = (j-1)\Delta x \tag{2.33}$$

to discrete wavenumber koordinates k_l

$$k_l = (l-1)\Delta k \tag{2.34}$$

Starting from equation (2.32) for the 1D case and substituting (2.33) and (2.34) in the trigonometric basis as:

$$e^{-i(\kappa_l x_j)} = e^{-i(2\pi k_l x_j)} = e^{-i(2\pi(l-1)\Delta k(j-1)\Delta x)} = e^{-i\frac{2\pi}{N}(l-1)(j-1)} \tag{2.35}$$

leads to:

$$\tilde{p}_m = \frac{1}{(2\pi)} \sum_{j=1}^{N} \hat{p}_j e^{-i\frac{2\pi}{N}(l-1)(j-1)} \Delta x_j \quad \text{vs} \quad \breve{p}_m = \frac{1}{N} \sum_{j=1}^{N} \hat{p}_j e^{-i\frac{2\pi}{N}(l-1)(j-1)} \tag{2.36}$$

On the equidistant array $\Delta x_j = \Delta x$ can be torn out of the sum and using $\Delta x = \frac{1}{N\Delta k}$ one gets:

$$\tilde{p}_m = \frac{1}{\Delta\kappa} \frac{1}{N} \sum_{j=1}^{N} \hat{p}_j e^{-i\frac{2\pi}{N}(l-1)(j-1)} \quad \text{vs} \quad \breve{p}_m = \frac{1}{N} \sum_{j=1}^{N} \hat{p}_j e^{-i\frac{2\pi}{N}(l-1)(j-1)} \tag{2.37}$$

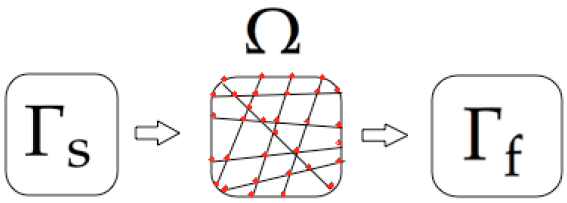

]

Fig. 2.5: *κ_s, x and κ_f regions*

The discrete values $\tilde{p}_m$ approximate the exact Fourier transform $\tilde{p}$ while $\check{p}$ yields the coefficients approximating the discrete Fourier transformation of $\hat{p}$. If the discrete values interpolating an exact Fourier transform are to be evaluated then the Fourier coefficients have to be scaled by wavenumber resolution $\Delta\kappa$ as:

$$\tilde{p} \approx \frac{\check{p}}{\Delta\kappa} \tag{2.38}$$

Note that a matrix $\boldsymbol{\mathcal{F}}$ with coefficients $f_{lj} = e^{-i\frac{2\pi}{N}(l-1)(j-1)}$ is usually referred to as the discrete Fourier transform matrix.

Infinite DAS is usually performed by choosing a desired focus wavenumber κ instead of restricting the range of possible focus wavenumbers to those required for the discrete duality relation $\boldsymbol{I} = \frac{1}{N}\boldsymbol{\mathcal{F}}^{-1}\boldsymbol{\mathcal{F}}$.

In case orthogonality holds for every projection of a single complex exponential $e^{i\kappa_s x}$ on another complex exponential $e^{-i\kappa_f x}$ the focus bases can be chosen arbitrarily.

$$\int_{x\in\mathbb{R}} e^{i\kappa_s x} e^{-i\kappa_f x} dx = 0 \quad \text{as long as} \quad \kappa_f \neq \kappa_s \tag{2.39}$$

Relation (2.39) is fulfilled only in the analytical case (integration over $\mathbb{R}$). In the discrete case

$$\sum_{x\in\Omega} e^{i\kappa_s x} e^{-i\kappa_f x} \Delta x \approx 0 \quad \text{for } \kappa_f \sim \kappa_s \quad \text{as long as} \quad \Omega \to \frac{1}{k_s} = \lambda_s \tag{2.40}$$

The bigger the array in comparison to λ_s the better orthogonality holds for focus wavenumbers close to κ_f.This is the reason for sidelobes appearing in iDAS as well as the Fourier transform. Additionally violation of Nyquist's criteria will result in aliasing. Conjugate symmetry between positive and negative focus wavenumber results from conjugate symmetric exponential bases.

The following conclusions can be drawn:

- The different algorithms result from different types of averaging:
  1. DAS $\Rightarrow$ ARITHMETIC averaging
  2. Fourier transform $\Rightarrow$ SPATIAL averaging
- The discrete Fourier transform can be interpreted as a functional DAS algorithm with weights reflecting the appropriate array length corresponding to each microphone
- For an equidistant array the iDAS algorithm equals the discrete Fourier transform from $\hat{p}(\boldsymbol{x}, \omega)$ to $\boldsymbol{\kappa} - \omega$ domain

c. The iDAS deconvolution problem

The relationship between iDAS and the measured pressures $\hat{p}(\boldsymbol{x}, \omega)$ has thoroughly been explained. The appearance of sidelobes in iDAS maps shall be adressed in this chapter by assuming a known source distribution $\tilde{p}(\boldsymbol{\kappa}_\mathrm{s}, \omega)$ depending on source wavenumbers $\boldsymbol{\kappa}_\mathrm{s}$ in wavenumber source space Γ_s that propagates into spatial domain Ω and is backpropagated towards a wavenumber focus space Γ_f through DAS. A simple sketch with arbitrary measuring coordinates $\boldsymbol{x}$ (red points) is provided in Figure 2.5.

The spatial pressure field measured at $\hat{p}(\boldsymbol{x}, \omega)$ ($\boldsymbol{x} \in \Omega_\mathrm{d} \subseteq \Omega$) consists only of plane waves $\tilde{p}_\mathrm{s}(\boldsymbol{\kappa}_\mathrm{s})$ at discrete wavenumber coordinates in subspace $\Gamma_{\mathrm{s|d}}$ ($\boldsymbol{\kappa}_\mathrm{s} \in \Gamma_{\mathrm{s|d}} \subseteq \Gamma_\mathrm{s}$) that can be localized as plane waves $\tilde{p}_\mathrm{f}(\boldsymbol{\kappa}_\mathrm{f})$ at focus wavenumbers $\Gamma_{\mathrm{f|d}}$ ($\boldsymbol{\kappa}_\mathrm{f} \in \Gamma_{\mathrm{f|d}} \subseteq \Gamma_\mathrm{f}$).

$$\hat{p}(\boldsymbol{x}, \omega) = \sum_{\boldsymbol{\kappa}_\mathrm{s} \in \Gamma_{\mathrm{s|d}}} \tilde{p}_\mathrm{s}(\boldsymbol{\kappa}_\mathrm{s}, \omega) e^{i\boldsymbol{\kappa}_\mathrm{s}\boldsymbol{x}} \tag{2.41}$$

Substituting $\hat{p}(\boldsymbol{x}, \omega)$ in the infinite DAS algorithm

$$\breve{p}_\mathrm{f}(\boldsymbol{\kappa}_\mathrm{f}, \omega) = \frac{1}{N} \sum_{x \in \Omega_\mathrm{d}} w(\boldsymbol{x}) \hat{p}(\boldsymbol{x}, \omega) e^{-i\boldsymbol{\kappa}_\mathrm{f}\boldsymbol{x}} \tag{2.42}$$

yields:

$$\breve{p}_\mathrm{f}(\boldsymbol{\kappa}_\mathrm{f}, \omega) = \frac{1}{N} \sum_{x \in \Omega_\mathrm{d}} w(\boldsymbol{x}) \sum_{\boldsymbol{\kappa}_\mathrm{s} \in \Gamma_{\mathrm{s|d}}} \tilde{p}_\mathrm{s}(\boldsymbol{\kappa}_\mathrm{s}, \omega) e^{i\boldsymbol{\kappa}_\mathrm{s}\boldsymbol{x}} e^{-i\boldsymbol{\kappa}_\mathrm{f}\boldsymbol{x}} \tag{2.43}$$

It is possible to rearrange the sum as:

$$\breve{p}_\mathrm{f}(\boldsymbol{\kappa}_\mathrm{f}, \omega) = \sum_{\boldsymbol{\kappa}_\mathrm{s} \in \Gamma_{\mathrm{s|d}}} \tilde{p}_\mathrm{s}(\boldsymbol{\kappa}_\mathrm{s}, \omega) \frac{1}{N} \sum_{x \in \Omega_\mathrm{d}} w(\boldsymbol{x}) e^{i\boldsymbol{x}(\boldsymbol{\kappa}_\mathrm{s} - \boldsymbol{\kappa}_\mathrm{f})} \tag{2.44}$$

By defining the iDAS point spread function $\breve{h}(\boldsymbol{\kappa}_\mathrm{s})$ (the convolution kernel) as

$$\breve{h}(\boldsymbol{\kappa}_\mathrm{s}) = \frac{1}{N} \sum_{x \in \Omega_\mathrm{d}} w(\boldsymbol{x}) e^{-i\boldsymbol{x}\boldsymbol{\kappa}_\mathrm{s}} \tag{2.45}$$

one can rewrite $\breve{p}(\boldsymbol{\kappa}_\mathrm{f}, \omega)$ as a discrete convolution product of the underlying source distribution $\tilde{p}(\boldsymbol{\kappa}_\mathrm{s}, \omega)$ with the shift-invariant iDAS point spread function

$$\breve{p}_\mathrm{f}(\boldsymbol{\kappa}_\mathrm{f}, \omega) = \tilde{p}_\mathrm{s}(\boldsymbol{\kappa}_\mathrm{s}, \omega) \bar{*} \breve{h}(\boldsymbol{\kappa}_\mathrm{s}) = \frac{1}{N} \sum_{\boldsymbol{x} \in \Omega_\mathrm{d} \tilde{p}_\mathrm{s}(\boldsymbol{\kappa}_\mathrm{s}, \omega)} \breve{h}(\boldsymbol{\kappa}_\mathrm{f} - \boldsymbol{\kappa}_\mathrm{s}) \tag{2.46}$$

The procedure is illustrated in Fig. 2.6. Assuming a single source impinging from orthogonal direction ($\kappa = 0$, Fig. 2.6a) on an equidistant array with diameter D and iDAS point-spread function as displayed in Fig. 2.6b than the measured signal becomes Fig. 2.6c.

In the equidistant case the unity weight iDAS PSF equals the discrete Fourier transform PSF and can (for a line array) be approximated as:

$$\breve{h}(\kappa_\mathrm{s}) = \frac{\sin(\kappa_\mathrm{s} D/2)}{\kappa_\mathrm{s} D/2} \quad \kappa \in \mathbb{R} \tag{2.47}$$

and for the circular array as Bessel function of order 1:

$$\breve{h}(\boldsymbol{\kappa}_\mathrm{s}) = \frac{\pi D}{|\boldsymbol{\kappa}_\mathrm{s}|} J_1(|\boldsymbol{\kappa}_\mathrm{s}| D/2) \quad \boldsymbol{\kappa}_\mathrm{s} \in \mathbb{R}^2 \tag{2.48}$$

Note that $\breve{h}(\boldsymbol{\kappa}_\mathrm{s})$ (2.45) for unity weights can also be referred to as the Dirichlet kernel which is defined as:

$$D_{\mathrm{n}}(\kappa) = \sum_{x=-n}^{n} e^{i\kappa x} \tag{2.49}$$

The point-spread function shape depends only on the array dimension but not on the sampling distance. This reflects the approximate validity of the orthogonality relation explained previously. A non-zero sampling distance results in aliasing above cutoff wavenumber $\kappa_{\mathrm{c}} = 2\pi\frac{1}{D}$ according to the sampling theorem.

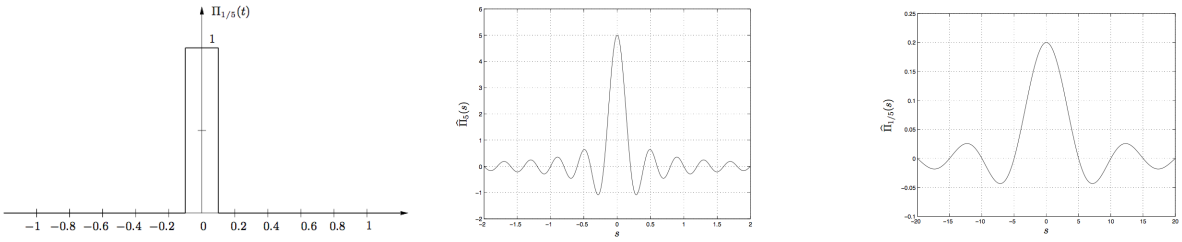

(a) *Plane wave at* $\boldsymbol{\kappa}_{\mathrm{s}} = 0$ **(b)** *Point-spread function* $\tilde{h}$ **(c)** *Observed signal*

Fig. 2.6: *Convolution illustration [22]*

A deconvolution attempt is a signal processing technique based on the following idea:

If $\check{p}_{\mathrm{f}}(\boldsymbol{\kappa}_{\mathrm{f}}, \omega)$ *can be evaluated from given microphone pressures* $\hat{p}(\boldsymbol{x}, \omega)$ *according to* (2.42) *and the point-spread function* $\check{h}(\boldsymbol{\kappa}_{\mathrm{s}})$ *can be evaluated according to* (2.45) *than it should be possible to extract the underlying source field* $\tilde{p}_{\mathrm{s}}(\boldsymbol{\kappa}_{\mathrm{s}}, \omega)$ *by solving equation* (2.46) *for* $\tilde{p}_{\mathrm{s}}(\boldsymbol{\kappa}_{\mathrm{s}}, \omega)$.

In practice (2.46) is ill-conditioned and can only be solved approximately in a least-squares sense. Additionally all measurements are polluted by noise that cannot be described as a single complex exponential (uncorrelated noise is no solution of Helmholtz's equation). This noise can thus not be represented as a convolution product with $\check{h}(\kappa_{\mathrm{s}})$ and becomes artificially magnified during the least-squares approximation. It is therefore common practice to solve the deconvolution problem not for measured pressures $\hat{p}(\boldsymbol{x}, \omega)$ but for the measured cross-power spectral density $\underline{S}(\boldsymbol{x}, \boldsymbol{\zeta}, \omega)$ or (under the assumption of incoherent sources) the shift-invariant cross power spectral density $S(\boldsymbol{\zeta}, \omega)$. This corresponds to a noise-minimization problem as will be explained later on. Infinite beamforming (a modification of iDAS) deconvolution for turbulent boundary layer measurements was for example applied in [11]. According to the considerations drawn in Subsection b it becomes clear that for the non-equidistant array case the wavenumber-frequency spectrum $\Phi(\boldsymbol{\kappa}, \omega)$ can only be evaluated in an energy-preserving way by taking into account the relative areas corresponding to each microphone. This becomes even more pronounced when a microphone array designed for wide variety of spatial separations is used which is exactly the case for the array used in this study. Arithmetic averaging overestimates spectral estimations for small correlation lengths resulting in an overestimated aerodynamic contribution compared with the desired acoustic contribution. Thus a formulation for the non-equidistant $\boldsymbol{\kappa} - \omega$ deconvolution problem was developed to extract the true source field $\tilde{\Phi}_{\mathrm{s}}(\boldsymbol{\kappa}_{\mathrm{s}}, \omega)$ underlying the non-equidistant spatial Fourier transform $\tilde{\Phi}_{\mathrm{f}}(\boldsymbol{\kappa}_{\mathrm{f}}, \omega)$ related to the cross-spectrum of $\hat{p}(\boldsymbol{x}, \omega)$. For simplicity the Fourier deconvolution problem is first derived for pressure but will later on also be applied on cross-power spectral density data.

d. The Fourier deconvolution problem

The Fourier deconvolution problem can easily be derived by remembering that the $\boldsymbol{\kappa} - \omega$ transformation can be interpreted as a functional beamformer with weights $w(\boldsymbol{x}) = \Delta A(\boldsymbol{x})$ reflecting the appropriate array area ΔA.The $\boldsymbol{\kappa} - \omega$ transformation algorithm

$$\tilde{p}_{\mathrm{f}}(\boldsymbol{\kappa}_{\mathrm{f}}, \omega) = \sum_{x \in \Omega_{\mathrm{d}}} \hat{p}(\boldsymbol{x}, \omega) e^{-i\boldsymbol{\kappa}_{\mathrm{f}}\boldsymbol{x}} \Delta A(\boldsymbol{x}) \tag{2.50}$$

can be expressed as a discrete convolution of the underlying source distribution $\tilde{p}_s(\boldsymbol{\kappa}_s, \omega)$ with the $\boldsymbol{\kappa} - \omega$ transformation PSF $\tilde{h}(\boldsymbol{\kappa}_s)$

$$\tilde{p}_f(\boldsymbol{\kappa}_f, \omega) = \tilde{p}_s(\boldsymbol{\kappa}_s, \omega) \overline{*} \tilde{h}(\boldsymbol{\kappa}_s) \tag{2.51}$$

where $\tilde{h}(\boldsymbol{\kappa}_s)$ follows from (2.45) with $w(\boldsymbol{x}) = \Delta A(\boldsymbol{x})$ to

$$\tilde{h}(\boldsymbol{\kappa}_s) = \sum_{x \in \Omega_d} e^{i\boldsymbol{x}\boldsymbol{\kappa}_s} \Delta A(\boldsymbol{x}) \tag{2.52}$$

e. The near-field deconvolution problem

A range of deconvolution algorithm (DAMAS,DAMAS2,CLEAN etc.) were developed especially for the deconvolution of near-field beamforming maps. It is thus deemed important to include a comprehensive derivation into this subject to allow cross-reading with the corresponding scientific papers.

It was shown previously that different propagator models can be used according to assumptions about the source field. If the source is not infinitely far away then the array pressure distribution in Ω can be calculated as a discrete convolution of the underlying source distribution $\hat{q}_s(\boldsymbol{x}_s, \omega)$ with Green's free-space function $G(\boldsymbol{x}_s, \omega)$ (see (2.28)). For $\boldsymbol{x}_s \in \Omega_{s|d} \subseteq \Omega_s$ (source domain), $\boldsymbol{x} \in \Omega_d \subseteq \Omega$ (measurement domain) and $\boldsymbol{x}_f \in \Omega_{f|d} \subseteq \Omega_f$ (focus domain) it follows that

$$\hat{p}(\boldsymbol{x}, \omega) = \sum_{\boldsymbol{x} \in \Omega_d} \hat{q}_s(\boldsymbol{x}_s) \frac{e^{i\omega|\boldsymbol{x} - \boldsymbol{x}_s|}}{|\boldsymbol{x} - \boldsymbol{x}_s|} = \hat{q}_s(\boldsymbol{x}_s, \omega) \overline{*} G(\boldsymbol{x}_s, \omega) \quad \text{with} \quad G(\boldsymbol{x}_s) = \frac{e^{i\omega|\boldsymbol{x}_s|}}{\boldsymbol{x}_s} \tag{2.53}$$

Green's free-space function is actually a zeroth order Bessel function of the first kind and thus (2.53) states that, similar to the Fourier transformation (with trigonometric bases) , $\hat{p}(\boldsymbol{x}, \omega)$ can be described as a series of zeroth order Bessel functions $G(\boldsymbol{x} - \boldsymbol{x}_s, \omega)$ with coefficients $\hat{q}_s(\boldsymbol{x}_s)$. Now , similar to analyze plane waves in $\boldsymbol{\kappa} - \omega$ space it is deemed beneficial to analyze spherical waves in a space made up by zeroth order Bessel function bases. Such a transformation is called a Hankel transformation of order zero and can be calculated by convolution of $\hat{p}(\boldsymbol{x}, \omega)$ with the inverse Green's function $G^{-1}(\boldsymbol{x}, \omega) = |\boldsymbol{x}| e^{-i\omega|\boldsymbol{x}|}$ (similar to the Fourier transform) :

$$q(\boldsymbol{x}_s) = \frac{1}{A} \hat{p}(\boldsymbol{x}, \omega) * G^{-1}(\boldsymbol{x}, \omega) = \frac{1}{A} \sum_{\boldsymbol{x} \in \Omega} \hat{p}(\boldsymbol{x}, \omega) |\boldsymbol{x}_f - \boldsymbol{x}| e^{-i\omega|\boldsymbol{x}_f - \boldsymbol{x}|} \Delta \boldsymbol{x} \tag{2.54}$$

Conversely, the conventional sDAS algorithm for pressure steering reads:

$$\breve{q}(\boldsymbol{x}_f, \omega) = \frac{1}{N} \sum_{\boldsymbol{x} \in \Omega} w(\boldsymbol{x}) \hat{p}(\boldsymbol{x}, \omega) |\boldsymbol{x}_f - \boldsymbol{x}| e^{-i\omega|\boldsymbol{x}_f - \boldsymbol{x}|} \tag{2.55}$$

Now one can compare the discretized spatial Hankel transformation and the conventional sDAS algorithm (unity weights $w(\boldsymbol{x}) = 1$) for pressure steering as:

$$\hat{q}_s(\boldsymbol{x}_s, \omega) = \frac{1}{A} \sum_{\boldsymbol{x} \in \Omega} \hat{p}(\boldsymbol{x}, \omega) |\boldsymbol{x}_f - \boldsymbol{x}| e^{-i\omega|\boldsymbol{x}_f - \boldsymbol{x}|} \Delta \boldsymbol{x} \quad \text{vs} \quad \breve{q}(\boldsymbol{x}_s, \omega) = \frac{1}{N} \sum_{\boldsymbol{x} \in \Omega} \hat{p}(\boldsymbol{x}, \omega) |\boldsymbol{x}_f - \boldsymbol{x}| e^{-i\omega|\boldsymbol{x}_f - \boldsymbol{x}|} \tag{2.56}$$

It becomes clear that similar to the relation between the $\boldsymbol{\kappa} - \omega$ transformation and the infinite Beamformer ((2.32)) the sDAS algorithm becomes a Hankel transformation only for an equidistant grid $\frac{\Delta x}{A} = \frac{1}{N}$. As spatial weighting yields considerable better performance in the plane wave case it is deemed a potentially fruitful attempt to weight microphone pressures with their affiliated surface area $\Delta \boldsymbol{x}$. This would break the mould of the current work and is therefore not considered here. The interested reader is invited to contact the author for further information. Instead the conventional pressure beamforming deconvolution procedure will be derived within this work. It is important to remember that conventional beamforming estimates the source strengh $\hat{q}_s(\boldsymbol{x}_s, \omega)$ based on an arithmetic averaging approach instead of the spatial averaging required for a Hankel transformation.

The conventional sDAS deconvolution problem can be derived by inserting the source field assumption $\hat{p}(\boldsymbol{x},\omega) = \hat{q}_\mathrm{s}(\boldsymbol{x}_\mathrm{s},\omega)\overline{*}G(\boldsymbol{x}_\mathrm{s},\omega)$ (2.53) into the sDAS algorithm for unity weights (2.56). It follows that:

$$\breve{q}(\boldsymbol{x}_\mathrm{f},\omega) = \frac{1}{N}\sum_{\boldsymbol{x}\in\Omega_\mathrm{d}}\sum_{\boldsymbol{x}_\mathrm{s}\in\Omega_{\mathrm{s}|\mathrm{d}}}\hat{q}_\mathrm{s}(\boldsymbol{x}_\mathrm{s},\omega)\frac{e^{i\omega|\boldsymbol{x}-\boldsymbol{x}_\mathrm{s}|}}{|\boldsymbol{x}-\boldsymbol{x}_\mathrm{s}|}e^{-i\omega|\boldsymbol{x}-\boldsymbol{x}_\mathrm{f}|}|\boldsymbol{x}-\boldsymbol{x}_\mathrm{f}| = \frac{1}{N}\left\{\{\hat{q}_\mathrm{s}(\boldsymbol{x}_\mathrm{s},\omega)\overline{*}G(\boldsymbol{x})\}\{\boldsymbol{x}_\mathrm{s}\}\overline{*}G^{-1}(\boldsymbol{x},\omega)\right\}\{\boldsymbol{x}\} \tag{2.57}$$

Rearranging allows to reformulate the problem as

$$\breve{q}(\boldsymbol{x}_\mathrm{f},\omega) = \sum_{\boldsymbol{x}_\mathrm{s}\in\Omega_{\mathrm{s}|\mathrm{d}}}\hat{q}_\mathrm{s}(\boldsymbol{x}_\mathrm{s},\omega)\sum_{\boldsymbol{x}\in\Omega_\mathrm{d}}\frac{1}{N}\frac{e^{i\omega|\boldsymbol{x}-\boldsymbol{x}_\mathrm{s}|}}{|\boldsymbol{x}-\boldsymbol{x}_\mathrm{s}|}e^{-i\omega|\boldsymbol{x}-\boldsymbol{x}_\mathrm{f}|}|\boldsymbol{x}-\boldsymbol{x}_\mathrm{f}| = \left\{\hat{q}_\mathrm{s}(\boldsymbol{x}_\mathrm{s},\omega) * \left\{G(\boldsymbol{x}-\boldsymbol{x}_\mathrm{s})\overline{*}G^{-1}(\boldsymbol{x})\right\}\{\boldsymbol{x}\}\right\}\{\boldsymbol{x}_\mathrm{s}\} \tag{2.58}$$

or by introducing the near-field point-spread function $\breve{h}_\mathrm{G}(\boldsymbol{x}_\mathrm{s},\boldsymbol{x}_\mathrm{f})$

$$\breve{h}_\mathrm{G}(\boldsymbol{x}_\mathrm{s},\boldsymbol{x}_\mathrm{f}) = \sum_{\boldsymbol{x}\in\Omega_\mathrm{d}}\frac{1}{N}\frac{e^{i\omega|\boldsymbol{x}-\boldsymbol{x}_\mathrm{s}|}}{|\boldsymbol{x}-\boldsymbol{x}_\mathrm{s}|}e^{-i\omega|\boldsymbol{x}-\boldsymbol{x}_\mathrm{f}|}|\boldsymbol{x}-\boldsymbol{x}_\mathrm{f}| = \{G(\boldsymbol{x}-\boldsymbol{x}_\mathrm{s})\overline{*}G(\boldsymbol{x})\}\{\boldsymbol{x}\} \tag{2.59}$$

one can finally formulate the near-field deconvolution problem as

$$\breve{q}(\boldsymbol{x}_\mathrm{f},\omega) = \sum_{\boldsymbol{x}_\mathrm{s}\in\Omega_{\mathrm{s}|\mathrm{d}}}\hat{q}_\mathrm{s}(\boldsymbol{x}_\mathrm{s},\omega)\breve{h}_\mathrm{G}(\boldsymbol{x}_\mathrm{s},\boldsymbol{x}_\mathrm{f}) = \left\{\hat{q}_\mathrm{s}(\boldsymbol{x}_\mathrm{s},\omega)\overline{*}_{|\mathrm{v}}\breve{h}_\mathrm{G}(\boldsymbol{x}_\mathrm{s},\boldsymbol{x}_\mathrm{f})\right\}\{\boldsymbol{x}_\mathrm{s}\} \tag{2.60}$$

Note that $\breve{h}_\mathrm{G}(\boldsymbol{x}_\mathrm{s},\boldsymbol{x}_\mathrm{f})$ cannot be written as $\breve{h}_\mathrm{G}(\boldsymbol{x}_\mathrm{s}-\boldsymbol{x}_\mathrm{f})$. The near-field point-spread function is therefore not shift-invariant. As a result (2.59) is a shift-variant convolution of $\hat{q}_\mathrm{s}(\boldsymbol{x}_\mathrm{s},\omega)$ with $\breve{h}_\mathrm{G}(\boldsymbol{x}_\mathrm{s},\boldsymbol{x}_\mathrm{f})$.

f. Trigonometric Interpolation

It has been shown that arbitrary measurements $\hat{p}(\boldsymbol{x},\omega)$ can be transformed into $\boldsymbol{\kappa}-\omega$ space by discretizing the Fourier convolution integral. If the pressure distribution $\hat{p}(\boldsymbol{x},\omega)$ follows from a physical phenomenon describable by plane waves then focus wavenumber $\boldsymbol{\kappa}_\mathrm{f}$ can be chosen arbitrarily. Now one can ask the following :

If $\tilde{p}(\boldsymbol{\kappa}_\mathrm{f},\omega) = \mathcal{F}\hat{p}(\boldsymbol{x},\omega)$ can be evaluated for every possible focus wavenumber $\boldsymbol{x}_\mathrm{f}$ then another variable $\hat{p}_{\bar{\mathrm{f}}}(\boldsymbol{x}_\mathrm{f},\omega)$ can be evaluated for every possible focus position $\boldsymbol{x}_\mathrm{f}\in\mathbb{R}^n$ as $\hat{p}_{\bar{\mathrm{f}}}(\boldsymbol{x}_\mathrm{f},\omega) = \mathcal{F}^{-1}\tilde{p}_\mathrm{f}(\boldsymbol{\kappa}_\mathrm{f},\omega)$. How is $\hat{p}_{\bar{\mathrm{f}}}(\boldsymbol{x}_\mathrm{f},\omega)$ related to $\hat{p}(\boldsymbol{x},\omega)$?

Discretizing the $\boldsymbol{x}-\omega$ transformation of $\tilde{p}_\mathrm{f}(\boldsymbol{\kappa}_\mathrm{f},\omega)$ with wavenumber domain weights $\Delta K(\boldsymbol{\kappa}_\mathrm{f})$ reflecting the wavenumber domain area belonging to each wavenumber coordinate $\boldsymbol{\kappa}_\mathrm{f}$ yields

$$\hat{p}_{\bar{\mathrm{f}}}(\boldsymbol{x}_\mathrm{f},\omega) = \sum_{\boldsymbol{\kappa}\in\Gamma_{\mathrm{f}|\mathrm{d}}}\tilde{p}(\boldsymbol{\kappa}_\mathrm{f},\omega)e^{i\boldsymbol{\kappa}_\mathrm{f}\boldsymbol{x}_\mathrm{f}}\Delta K(\boldsymbol{\kappa}_\mathrm{f}) \tag{2.61}$$

and by pointing out that $\tilde{p}_\mathrm{f}(\boldsymbol{\kappa}_\mathrm{f},\omega)$ was originally evaluated as:

$$\tilde{p}_{\boldsymbol{f}}(\boldsymbol{\kappa}_\mathrm{f},\omega) = \sum_{x\in\Omega_\mathrm{d}}\hat{p}(\boldsymbol{x},\omega)e^{-i\boldsymbol{\kappa}_\mathrm{f}\boldsymbol{x}}\Delta A(\boldsymbol{x}) \tag{2.62}$$

one can rewrite $\hat{p}_{\bar{\mathrm{f}}}(\boldsymbol{x}_\mathrm{f},\omega)$ as

$$\hat{p}_{\bar{\mathrm{f}}}(\boldsymbol{x}_\mathrm{f},\omega) = \sum_{\boldsymbol{\kappa}\in\Gamma_{\mathrm{f}|\mathrm{d}}}\sum_{x\in\Omega_\mathrm{d}}\hat{p}(\boldsymbol{x},\omega)e^{i\boldsymbol{\kappa}_\mathrm{f}\boldsymbol{x}_\mathrm{f}}e^{-i\boldsymbol{\kappa}_\mathrm{f}\boldsymbol{x}}\Delta A(\boldsymbol{x})\Delta K(\boldsymbol{\kappa}_\mathrm{f}) \tag{2.63}$$

By defining the Fourier interpolation kernel $\overline{h}(\boldsymbol{x})$ as

$$\overline{h}(\boldsymbol{x}) = \sum_{\boldsymbol{\kappa} \in \Gamma_{\mathrm{f|d}}} e^{i\boldsymbol{\kappa}_{\mathrm{f}}\boldsymbol{x}} \Delta K(\boldsymbol{\kappa}_{\mathrm{f}}) \tag{2.64}$$

one can express the resampled pressures $\hat{p}_{\bar{\mathrm{f}}}(\boldsymbol{x}_{\mathrm{f}}, \omega)$ as

$$\hat{p}_{\bar{\mathrm{f}}}(\boldsymbol{x}_{\mathrm{f}}, \omega) = \sum_{x \in \Omega_{\mathrm{d}}} \hat{p}(\boldsymbol{x}, \omega) \overline{h}(\boldsymbol{x}_{\mathrm{f}} - \boldsymbol{x}) \Delta A(\boldsymbol{x}) = \hat{p}(\boldsymbol{x}, \omega) \overline{*} \overline{h}(\boldsymbol{x}) \tag{2.65}$$

The backtransformation seemingly allows to calculate the measured pressures on arbitrary coordinates $\boldsymbol{x}_{\mathrm{f}}$. This can directly be explained by the Fourier transformation whose most fundamental assumption is that the whole field $\hat{p}(\boldsymbol{x}, \omega)$ can be expressed through a trigonometric series with coefficients $\tilde{p}_{\mathrm{f}}(\boldsymbol{\kappa}_{\mathrm{f}}, \omega)$. By remembering that the $\boldsymbol{\kappa} - \omega$ transformation result $\tilde{p}_{\mathrm{f}}(\boldsymbol{\kappa}_{\mathrm{f}}, \omega)$ of a single source $\tilde{p}_{\mathrm{s}}(\boldsymbol{\kappa}_{\mathrm{s}}, \omega)$ becomes the Fourier PSF $\tilde{h}(\boldsymbol{\kappa}_{\mathrm{f}})$ and the finite backtransformation of $\tilde{h}(\boldsymbol{\kappa}_{\mathrm{f}})$ does not consist of a single plane wave but also from contributions from sidelobes it can be concluded that $\hat{p}_{\bar{\mathrm{f}}}(\boldsymbol{x}_{\mathrm{f}}, \omega)$ is only a polluted interpolation of the underlying spatial field. In case the underlying source field $\tilde{p}_{\mathrm{s}}(\boldsymbol{\kappa}_{\mathrm{s}}, \omega)$ is known it becomes possible to calculate the measured pressures on arbitrary coordinates $\boldsymbol{x}_{\mathrm{f}}$ without the sidelobes resulting from limited array size. Solving the deconvolution problem

$$\tilde{p}_{\mathrm{f}}(\boldsymbol{\kappa}_{\mathrm{f}}, \omega) = \tilde{p}_{\mathrm{s}}(\boldsymbol{\kappa}_{\mathrm{s}}, \omega) \overline{*} \tilde{h}(\boldsymbol{\kappa}_{\mathrm{s}}, \omega) \tag{2.66}$$

and transforming the resulting signal $\tilde{p}_{\mathrm{f}}(\boldsymbol{\kappa}_{\mathrm{f}}, \omega)$ back on arbitrary focus coordinates $\boldsymbol{x}_{\mathrm{f}}$ as

$$\hat{p}_{\bar{\mathrm{f}}}(\boldsymbol{x}_{\mathrm{f}}, \omega) = \sum_{\boldsymbol{\kappa} \in \Gamma_{\mathrm{s|d}}} \tilde{p}_{\mathrm{s}}(\boldsymbol{\kappa}_{\mathrm{s}}, \omega) e^{i\boldsymbol{\kappa}_{\mathrm{s}}\boldsymbol{x}_{\mathrm{s}}} \Delta \boldsymbol{K}(\boldsymbol{\kappa}_{\mathrm{s}}) \tag{2.67}$$

can therefore be seen as a trigonometric best-fit interpolation of $\hat{p}(\boldsymbol{x}, \omega)$ in a least-squares sense. The trigonometric fit is not limited to the original measuring space $\boldsymbol{\Omega}_{\mathrm{d}}$ but can be evaluated on all coordinates within $\mathbb{R}^n$. Noting that the shape of the point-spread function stems from the spatial limitations of the measuring array and becomes a δ-function in case of unlimited array size it can be concluded that solving the deconvolution problem can also be interpreted as reconstructing the total source field on $\mathbb{R}^n$ which is in theory possible as long as all wavenumbers are measured (Nyquist) and included in $\Gamma_{\mathrm{f|d}}$ space.

g. Spherical interpolation

The same conclusion drawn for plane waves can similarly be drawn for spherical waves. If $\hat{q}_{\mathrm{s}}(\boldsymbol{x}_{\mathrm{s}}, \omega)$ is known and the desired interpolation coordinates are $\boldsymbol{x}_{\bar{\mathrm{f}}}$ than the least-squares spherical wave interpolation $\hat{p}_{\bar{\mathrm{f}}}(\boldsymbol{x}_{\bar{\mathrm{f}}}, \omega)$ becomes

$$p_{\bar{\mathrm{f}}}(\boldsymbol{x}_{\mathrm{f}}, \omega) = \sum_{\boldsymbol{x}_{\mathrm{s}} \in \Omega_{\mathrm{s|d}}} \hat{q}_{\mathrm{s}}(\boldsymbol{x}_{\mathrm{s}}, \omega) \frac{e^{i\omega|\boldsymbol{x}_{\mathrm{f}} - \boldsymbol{x}_{\mathrm{s}}|}}{|\boldsymbol{x}_{\bar{\mathrm{f}}} - \boldsymbol{x}_{\mathrm{s}}|} = \left\{ \hat{q}_{\mathrm{s}}(\boldsymbol{x}_{\mathrm{s}}, \omega) \overline{*} G(\boldsymbol{x}_{\underline{\mathrm{S}}}, \omega) \right\} \{\boldsymbol{x}_{\mathrm{s}}\} \tag{2.68}$$

h. Vectorized Notation

The following section will define vectors and matrices that allow to efficiently calculate the necessary sums for iDAS, the $\boldsymbol{\kappa} - \omega$ transformation and the sDAS algorithm in vectorized notation.

For an assumed equidistant one-dimensional source and focus grid with M wavenumber coordinates $\kappa_{\mathrm{s}}, \kappa_{\mathrm{f}} \in \Gamma_{\mathrm{s|d}}$ and an arbitrary line array with N microphones with coordinates $\boldsymbol{x} \in \Omega_{\mathrm{d}}$ we define (as common in literature) the spectral steering matrix $\boldsymbol{E}$ with coefficients $e_{jl} = e^{i\kappa_l x_j}$ and the spatial steering matrix $\boldsymbol{G}$ (corresponding to Green's function) with coefficients $g_{jl} = \frac{1}{x_j - x_l} e^{-i\omega|x_j - x_l|}$ as well as the inverse spatial steering matrix $\boldsymbol{G}^{\mathrm{i}}$ with coefficients $g^{\mathrm{i}}_{lj} = |x_j - x_l| e^{i\omega|x_j - x_l|}$. Then one can apply the vectorized unity weight DAS algorithm on pressure vector $\hat{\boldsymbol{p}}$ with coordinates $\boldsymbol{x}$ at frequency ω the following:

Conventional infinite pressure beamforming

$$\breve{p}_\mathrm{f}(\boldsymbol{\kappa}_\mathrm{f},\omega) = \frac{1}{N}\sum_{\boldsymbol{x}\in\Omega_\mathrm{d}} \hat{p}(\boldsymbol{x},\omega)e^{-i\boldsymbol{\kappa}_\mathrm{f}\boldsymbol{x}} \Rightarrow \breve{\boldsymbol{p}}_\mathrm{f} = \frac{1}{N}\boldsymbol{E}^H\hat{\boldsymbol{p}} \tag{2.69}$$

$$\breve{p}_\mathrm{f}(\boldsymbol{\kappa}_\mathrm{f},\omega) = \sum_{\boldsymbol{\kappa}_\mathrm{s}\in\Gamma_{\mathrm{s|d}}} \tilde{p}_\mathrm{s}(\boldsymbol{\kappa}_\mathrm{s},\omega)\tilde{h}(\boldsymbol{\kappa}_\mathrm{f}-\boldsymbol{\kappa}_\mathrm{s}) \Rightarrow \breve{\boldsymbol{p}}_\mathrm{f} = \breve{\boldsymbol{H}}\tilde{\boldsymbol{p}}_\mathrm{s} \tag{2.70}$$

with point-spread matrix $\breve{\boldsymbol{H}}$ defined as:

$$\breve{h}(\boldsymbol{\kappa}_\mathrm{f}-\boldsymbol{\kappa}_\mathrm{s}) = \frac{1}{N}\sum_{\boldsymbol{x}\in\Omega_\mathrm{d}} e^{-i(\boldsymbol{\kappa}_\mathrm{f}-\boldsymbol{\kappa}_\mathrm{s})\boldsymbol{x}} \Rightarrow \breve{\boldsymbol{H}} = \frac{1}{N}\boldsymbol{E}^H\boldsymbol{E} \tag{2.71}$$

The point spread matrix $\breve{\boldsymbol{H}}$ contains in each row f the iDAS response for a unity strength source at position $\boldsymbol{\kappa}_{\mathrm{s|f}}$. Shift invariance allows to calculate the full matrix by shifting the response for the first assumed source position. Another possibility is to calculate the kernel and perform the MATLAB builtin convolution operations (much faster). The kernel calculates as $\breve{\boldsymbol{h}} = \frac{1}{N}\boldsymbol{E}^H\boldsymbol{E}(:,(N+1)/2)$.

Wavenumber-frequency transformation

$$\tilde{p}_\mathrm{f}(\boldsymbol{\kappa}_\mathrm{f},\omega) = \frac{1}{N}\sum_{\boldsymbol{x}\in\Omega_\mathrm{d}} \hat{p}(\boldsymbol{x},\omega)e^{-i\boldsymbol{\kappa}_\mathrm{f}\boldsymbol{x}}\Delta\boldsymbol{x} \Rightarrow \tilde{\boldsymbol{p}}_\mathrm{f} = \frac{1}{N}\boldsymbol{E}^H(\hat{\boldsymbol{p}}\circ\Delta\boldsymbol{x}) \tag{2.72}$$

$$\tilde{p}_\mathrm{f}(\boldsymbol{\kappa}_\mathrm{f},\omega) = \sum_{\boldsymbol{\kappa}_\mathrm{s}\in\Gamma_{\mathrm{s|d}}} \tilde{p}_\mathrm{s}(\boldsymbol{\kappa}_\mathrm{s},\omega)\tilde{h}(\boldsymbol{\kappa}_\mathrm{f}-\boldsymbol{\kappa}_\mathrm{s}) \Rightarrow \tilde{\boldsymbol{p}}_\mathrm{f} = \tilde{\boldsymbol{H}}\tilde{\boldsymbol{p}}_\mathrm{s} \tag{2.73}$$

with point-spread matrix $\tilde{\boldsymbol{H}}$ defined as:

$$\tilde{h}(\boldsymbol{\kappa}_\mathrm{f}-\boldsymbol{\kappa}_\mathrm{s}) = \frac{1}{N}\sum_{\boldsymbol{x}\in\Omega_\mathrm{d}} e^{-i(\boldsymbol{\kappa}_\mathrm{f}-\boldsymbol{\kappa}_\mathrm{s})\boldsymbol{x}}\Delta\boldsymbol{x} \Rightarrow \tilde{\boldsymbol{H}} = \frac{1}{N}\boldsymbol{E}^H(\boldsymbol{E}\circ\boldsymbol{\Delta}) \tag{2.74}$$

Matrix $\boldsymbol{\Delta}$ contains M columns of vector $\boldsymbol{\Delta x}$.

Nearfield beamforming

The unity weight sDAS algorithm can be vectorized the following:

$$\breve{q}_\mathrm{f}(\boldsymbol{x}_\mathrm{f},\omega) = \frac{1}{N}\hat{p}(\boldsymbol{x},\omega)|\boldsymbol{x}_\mathrm{f}-\boldsymbol{x}|e{-}i\kappa_0|\boldsymbol{x}_\mathrm{f}-\boldsymbol{x}| \Rightarrow \breve{\boldsymbol{q}} = \frac{1}{N}\boldsymbol{G}^\mathrm{i}\hat{\boldsymbol{p}} \tag{2.75}$$

Its relation to the underlying source field $\hat{q}_\mathrm{s}$ becomes:

$$\breve{q}(\boldsymbol{x}_\mathrm{f},\omega) = \sum_{\boldsymbol{x}_\mathrm{s}\in\Omega_{\mathrm{s|d}}} \hat{q}_\mathrm{s}(\boldsymbol{x}_\mathrm{s},\omega)\breve{h}_\mathrm{G}(\boldsymbol{x}_\mathrm{s},\boldsymbol{x}_\mathrm{f}) = \left\{\hat{q}_\mathrm{s}(\boldsymbol{x}_\mathrm{s},\omega)\overline{*}_{|\mathrm{v}}\breve{h}_\mathrm{G}(\boldsymbol{x}_\mathrm{s},\boldsymbol{x}_\mathrm{f})\right\}\{\boldsymbol{x}_\mathrm{s}\} \Rightarrow \breve{\boldsymbol{q}}_\mathrm{f} = \breve{\boldsymbol{H}}_\mathrm{G}\hat{\boldsymbol{q}}_\mathrm{s} \tag{2.76}$$

with the near-field point-spread matrix

$$\breve{h}_\mathrm{G}(\boldsymbol{x}_\mathrm{s},\boldsymbol{x}_\mathrm{f}) = \sum_{\boldsymbol{x}\in\Omega_\mathrm{d}} \frac{1}{N}\frac{e^{i\omega|\boldsymbol{x}-\boldsymbol{x}_\mathrm{s}|}}{|\boldsymbol{x}-\boldsymbol{x}_\mathrm{s}|}e^{-i\omega|\boldsymbol{x}-\boldsymbol{x}_\mathrm{f}|}|\boldsymbol{x}-\boldsymbol{x}_\mathrm{f}| = \frac{1}{N}\left\{G(\boldsymbol{x}-\boldsymbol{x}_\mathrm{s})\overline{*}G(\boldsymbol{x})\right\}\{\boldsymbol{x}\} \Rightarrow \breve{\boldsymbol{H}}_\mathrm{G} = \frac{1}{N}\boldsymbol{G}^\mathrm{i}\boldsymbol{G} \tag{2.77}$$

In case of two dimensional array structure index transformation has to be applied to transform matrices into vectors. Afterwards the calculations can be performed equally.

IV. Cross-power Beamforming

The previous algorithms (iDAS, sDAS, $\kappa - \omega$ were all attempting to estimate amplitude and phase of the incoming wave. The usual center of interest of scientists and engineers is not amplitude and phase but only the POWER of the incoming wave. Algorithms estimating this power stem directly from the previously explained ones:

- iDAS $\Rightarrow$ infinite beamforming
- sDAS $\Rightarrow$ conventional beamforming
- $\kappa - \omega$ transformation $\Rightarrow$ $\kappa - \omega$ power transformation

The power can be calculated directly by taking the trace of the cross-power spectral density resulting from amplitude algorithms. A big benefit of this method is that uncorrelated noise becomes minimized allowing a better identification of the waves. Coherency information can also be gained by using the out-of-diagonal terms. The derivations are shown for a 1D array but can easily be adapted for a higher dimensional case using index transformation.

a. Infinite power Beamformer

In order to obtain the beamformed power for the plane wave DAS algorithm one has to calculate the beamformed Cross-Correlation map $\breve{\underline{\boldsymbol{\Phi}}}$.

Starting from (2.69) and multiplying it with its transpose-only gives:

$$\breve{\boldsymbol{p}} = \frac{1}{N}\boldsymbol{E}^H\hat{\boldsymbol{p}} \Rightarrow \breve{\boldsymbol{p}}\breve{\boldsymbol{p}}^H = \frac{1}{N^2}\boldsymbol{E}^H\hat{\boldsymbol{p}}(\boldsymbol{E}^H\hat{\boldsymbol{p}})^H = \frac{1}{N^2}\boldsymbol{E}^H\hat{\boldsymbol{p}}\hat{\boldsymbol{p}}^H\boldsymbol{E} \tag{2.78}$$

$$\breve{\underline{\boldsymbol{\Phi}}} = \frac{1}{N^2}\boldsymbol{E}^H\underline{\boldsymbol{S}}\boldsymbol{E} \tag{2.79}$$

Term $\breve{\underline{\boldsymbol{\Phi}}}$ is the full beamformed wavenumber-frequency spectrum. A 4D wavespace coherent deconvolution approach for the equidistant $\boldsymbol{\kappa} - \omega$ transformation was presented by Chris Bahr in [2]. As explained previously the infinite Beamformer follows the same path by taking an arithmetic average instead of the spatial average. The full spectrum can be used to analyze coherence of multiple sources. If the shift invariance assumption holds and $\underline{S}(\boldsymbol{x}, \boldsymbol{\zeta}, \omega) = S(\boldsymbol{\zeta}, \omega)$ then $\boldsymbol{s}$ is sufficient to describe the whole cross-power density spectrum. Rewriting (2.79) in index notation shows how the resulting shift-invariant beamformed wavenumber-frequency spectrum $\breve{\boldsymbol{\Phi}}$ can be calculated from the shift-invariant cross-power spectral density vector $\boldsymbol{s}$:

$$\breve{\underline{\Phi}}_{l'l} = \frac{1}{N^2}\sum_{j'=1}^{N} e^{-i\kappa_{l'}x'_j}\sum_{j=1}^{N}\underline{S}_{j'j}e^{-i\kappa_l x_j} = \frac{1}{N^2}\sum_{j'=1}^{N}\sum_{j=1}^{N}\underline{S}_{j'j}e^{-i(\kappa_l x_j + \kappa_{l'}x_{j'})} \tag{2.80}$$

By taking a reference microphone with coordinate $x = 0$ at $j' = 1$ and the corresponding row $\underline{S}_{1j}$ one obtains

$$\breve{\underline{\Phi}}_{ll} = \frac{1}{N^2}\sum_{j=1}^{N}\underline{S}_{1j}e^{-i\kappa_l x_j} \quad or \quad \breve{\boldsymbol{\Phi}} = \frac{1}{N^2}\boldsymbol{E}^H\boldsymbol{s} \tag{2.81}$$

The PSF remains the one given for the iDAS beamformer $\breve{\boldsymbol{H}}$ in equation (2.71).

b. The wavenumber-frequency transformation for cross-power spectral data

Similar derivations can be provided for the $\boldsymbol{\kappa} - \omega$ transformation by starting from (2.72) :

$$\tilde{\boldsymbol{p}} = \boldsymbol{E}^H(\hat{\boldsymbol{p}} \circ \boldsymbol{\Delta x}) \Rightarrow \tilde{\boldsymbol{p}}\tilde{\boldsymbol{p}}^H = \boldsymbol{E}^H(\hat{\boldsymbol{p}} \circ \boldsymbol{\Delta x})[\boldsymbol{E}^H(\hat{\boldsymbol{p}} \circ \boldsymbol{\Delta x})]^H = \boldsymbol{E}^H(\hat{\boldsymbol{p}} \circ \boldsymbol{\Delta x})(\tilde{\boldsymbol{p}} \circ \boldsymbol{\Delta x})^H\boldsymbol{E}) \tag{2.82}$$

$$\tilde{\boldsymbol{p}}\tilde{\boldsymbol{p}}^H = \boldsymbol{E}^H[(\hat{\boldsymbol{p}}\hat{\boldsymbol{p}}^H) \circ (\boldsymbol{\Delta x}\boldsymbol{\Delta x}^{\boldsymbol{H}})]\boldsymbol{E} \tag{2.83}$$

$$\underline{\tilde{\mathbf{\Phi}}} = \boldsymbol{E}^H[\underline{\boldsymbol{S}} \circ (\boldsymbol{\Delta x}\boldsymbol{\Delta x}^H)]\boldsymbol{E} \tag{2.84}$$

where $\underline{\tilde{\mathbf{\Phi}}}$ denotes the full fourier transformed wavenumber-frequency spectrum.
For the shift invariant case one arrives at:

$$\tilde{\mathbf{\Phi}} = \frac{1}{N^2}\boldsymbol{E}^H(\boldsymbol{s} \circ \boldsymbol{\Delta} x) \tag{2.85}$$

As for DAS the point-spread function $\tilde{\boldsymbol{H}}$ remains the same as given for the $\boldsymbol{\kappa} - \omega$ transformation ((2.74)).

c. Near-field power Beamformer

For the near-field cross-power beamformer the source correlation map $\underline{\breve{\mathbf{\Theta}}}$ becomes (by starting from (2.75)):

$$\breve{\boldsymbol{q}}\breve{\boldsymbol{q}}^H = \boldsymbol{G}^{\mathrm{i}}\hat{\boldsymbol{p}}(\boldsymbol{G}^{\mathrm{i}}\hat{\boldsymbol{p}})^H = \boldsymbol{G}^{\mathrm{i}}\hat{\boldsymbol{p}}\hat{\boldsymbol{p}}^H\boldsymbol{G}^{\mathrm{i}^H} \tag{2.86}$$

$$\underline{\breve{\mathbf{\Theta}}} = \boldsymbol{G}^{\mathrm{i}}\underline{\boldsymbol{S}}\boldsymbol{G}^{\mathrm{i}^H} \tag{2.87}$$

In general core interest lies only in the beamformed source auto-power $\langle \boldsymbol{q} \rangle^2$ stored in the diagonal of $\underline{\breve{\mathbf{\Theta}}}$ ($\breve{\boldsymbol{q}} = trace(\underline{\breve{\mathbf{\Theta}}})$). Therefore only $\underline{\breve{\Theta}}_{ll}$ has to be calculated. Rewriting (2.87) shows

$$\underline{\breve{\Theta}}_{l'l} = \sum_{j=1}^{N}\sum_{j'=1}^{N}\underline{S}_{j'j}|x_l - x_j||x_{l'} - x_{j'}|e^{-i\omega|x_l - x_j|}e^{i\omega|x_{l'} - x_{j'}|} \tag{2.88}$$

for $l = l'$

$$\underline{\breve{\Theta}}_{ll} = \sum_{j=1}^{N}\sum_{j'=1}^{N}\underline{S}_{j'j}|x_l - x_j||x_l - x_{j'}|e^{-i\omega|x_l - x_j|}e^{i\omega|x_l - x_{j'}|} \tag{2.89}$$

$$\underline{\breve{\Theta}}_{ll} = \sum_{j=1}^{N}|x_l - x_{j'}|e^{i\omega|x_l - x_{j'}|}\sum_{j'=1}^{N}\underline{S}_{j'j}|x_l - x_j|e^{-i\omega|x_l - x_j|} = \sum_{j=1}^{N}g_{lj'}^{\mathrm{i}^*}\sum_{j'=1}^{N}g_{lj}^{\mathrm{i}}S_{j'j} \tag{2.90}$$

or in matrix notation

$$\underline{\breve{q}}_l = \boldsymbol{g}_l^{\mathrm{i}^H}\underline{\boldsymbol{S}}\boldsymbol{g}_l^{\mathrm{i}} \tag{2.91}$$

where $\boldsymbol{g}_l$ denotes the column vector of all components of $\boldsymbol{G}$ in row l.
(2.91) is a common notation to calculate the output power spectrum for near-field beamforming. It can be found for example in [5]. The cross-power point spread function for the underlying auto-power vector $\boldsymbol{q}_{\mathrm{s}}$ can be derived by calculating an artificial cross-spectral density matrix for an assumed source region. The pressure resulting from a discrete source power distribution $\hat{q}_{\mathrm{s}}$ can be derived by starting with:

Now by neglecting coherence information one can calculate a beamformed map by taking only the auto-power contribution $\langle \breve{\boldsymbol{q}} \rangle^2$ stored in the diagonal of $\underline{\breve{\mathbf{\Theta}}}$ ($\langle \breve{\boldsymbol{q}} \rangle^2 = \underline{\breve{\boldsymbol{q}}} = trace(\underline{\breve{\mathbf{\Theta}}})$). Rewriting (26) in index notation shows

$$\underline{\breve{\Theta}}_{l'l} = \sum_{j=1}^{N}\sum_{j'=1}^{N}\underline{S}_{j'j}|x_l - x_j||x_{l'} - x_{j'}|e^{-i\kappa_0|x_l - x_j|}e^{i\kappa_0|x_{l'} - x_{j'}|} \tag{2.92}$$

for $l = l'$

$$\underline{\breve{\Theta}}_{ll} = \sum_{j=1}^{N}\sum_{j'=1}^{N}\underline{S}_{j'j}|x_l - x_j||x_l - x_{j'}|e^{-i\kappa_0|x_l - x_j|}e^{i\kappa_0|x_l - x_{j'}|} \tag{2.93}$$

$$\underline{\breve{\Theta}}_{ll} = \sum_{j=1}^{N} |x_l - x_j| e^{i\kappa_0 |x_l - x_j|} \sum_{j'=1}^{N} \underline{S}_{j'j} |x_l - x'_j| e^{-i\kappa_0 |x_l - x'_j|} \tag{2.94}$$

$$\underline{\breve{\Theta}}_{ll} = \sum_{j=1}^{N} g_{lj'}^{\mathrm{i}^*} \sum_{j'=1}^{N} g_{lj}^{\mathrm{i}} \underline{S}_{j'j} \tag{2.95}$$

or in matrix notation

$$\underline{\breve{q}}_l = \boldsymbol{g}_l^{\mathrm{i}^H} \underline{\boldsymbol{S}} \boldsymbol{g}_l^{\mathrm{i}} \tag{2.96}$$

where $\boldsymbol{g}_l$ denotes the column vector of all components of $\boldsymbol{G}$ in row l.

The corresponding deconvolution problem can be derived by applying the algorithm on an artificial cross-power spectral density matrix resulting from an unknown discrete source power distribution $\hat{\boldsymbol{q}}_{\mathbf{s}}$. First we assume a single source at $\boldsymbol{x}_{\mathrm{s|i}}$. The obtained pressure vector $\hat{\boldsymbol{p}}_i$ becomes:

$$\hat{\boldsymbol{p}}_i = \boldsymbol{g}_i \hat{q}_{\mathrm{s|i}} \tag{2.97}$$

Using the definition of the squared auto-power one can calculate the artificial cross-power spectral matrix $\boldsymbol{S}_{\mathrm{i}}$.

$$\underline{\boldsymbol{S}}_i = \hat{\boldsymbol{p}}_i \hat{\boldsymbol{p}}_i^H = \boldsymbol{g}_i \hat{q}_{\mathrm{s|i}} (\boldsymbol{g}_i \hat{q}_{\mathrm{s|i}})^H = \boldsymbol{g}_i \hat{q}_{\mathrm{s|i}} \hat{q}_{\mathrm{s|i}}^H \boldsymbol{g}_i^H \tag{2.98}$$

$$\underline{\boldsymbol{S}}_i = \boldsymbol{g}_i \boldsymbol{g}_i^H \underline{\hat{q}}_{\mathrm{s|i}} \tag{2.99}$$

Now by applying (2.91) on $\underline{\boldsymbol{S}}_i$ one can express the beamforming map entry $\underline{\breve{q}}_{i|l}$ at position $\boldsymbol{x}_{\mathrm{f|l}}$ resulting from a single source situated at $\boldsymbol{x}_{\mathrm{s|i}}$ as:

$$\underline{\breve{q}}_{i|l} = \boldsymbol{g}_l^{\mathrm{i}^H} \boldsymbol{g}_i \boldsymbol{g}_i^H \underline{\hat{q}}_{\mathrm{s|i}} \boldsymbol{g}_l^{\mathrm{i}} = \boldsymbol{g}_l^{\mathrm{i}^H} \boldsymbol{g}_i \boldsymbol{g}_i^H \boldsymbol{g}_l^{\mathrm{i}} \underline{\hat{q}}_{\mathrm{s|i}} \tag{2.100}$$

It turns out that instead of performing a loop for each index l the computation can be more efficiently evaluated the following:

$$\underline{\breve{\boldsymbol{q}}}_i = \boldsymbol{G}^{\mathrm{i}^H} \boldsymbol{g}_i \boldsymbol{g}_i^H \boldsymbol{G}^{\mathrm{i}} \underline{\hat{q}}_{\mathrm{s|i}} \tag{2.101}$$

Now we can calculate the beamforming map resulting from a superposition of M individual sources by summing up over the individual contributions.

$$\underline{\breve{\boldsymbol{q}}} = \sum_{i=1}^{M} \boldsymbol{G}^{\mathrm{i}^H} \boldsymbol{g}_i \boldsymbol{g}_i^H \boldsymbol{G}^{\mathrm{i}} \underline{\hat{q}}_{\mathrm{s|i}} \tag{2.102}$$

The summation can also be evaluated as:

$$\underline{\breve{\boldsymbol{q}}} = \boldsymbol{G}^{\mathrm{i}^H} \boldsymbol{G} \boldsymbol{G}^H \boldsymbol{G}^{\mathrm{i}} \underline{\hat{\boldsymbol{q}}}_{\mathrm{s}} = \underline{\breve{\boldsymbol{H}}} \underline{\hat{\boldsymbol{q}}}_{\mathrm{s}} \tag{2.103}$$

The discrete shift-invariant convolution in (2.60) is performed by multiplying the point-spread matrix $\underline{\breve{\boldsymbol{H}}}$ with the source vector $\underline{\hat{\boldsymbol{q}}}_{\mathrm{s}}$. The translated kernel is stored in the rows of $\underline{\breve{\boldsymbol{H}}}$.

d. Summary: Deconvolution problems in array processing

For completeness the three most common cross-power algorithms are summarized here in matrix notation:

For a grid with M grid points in the underlying source region Γ_{s} (regardless if in κ- or x-space) and N microphones at position $\boldsymbol{x}_j$ one defines the following matrices:

- $\boldsymbol{E} \Rightarrow e_{jl} = e^{i\kappa_k x_j}$ with $dim(\boldsymbol{E}) = [N\,x\,M]$
- $\boldsymbol{G} \Rightarrow g_{jl} = \frac{1}{|\boldsymbol{x}_j - \boldsymbol{x}_l|} e^{-} i\omega |x_j - x_l|$ with $dim(\boldsymbol{G}) = [N\,x\,M]$
- $\boldsymbol{G}^{\mathrm{i}} \Rightarrow g^{\mathrm{i}}_{lj} = |\boldsymbol{x}_j - \boldsymbol{x}_l| e^{i\omega|x_j - x_l|}$ with $dim(\boldsymbol{G}^{\mathrm{i}}) = [M\,x\,N]$
- $\boldsymbol{g}^{\mathrm{i}}_l$ with $g^{\mathrm{i}}_{l|j} = g^{\mathrm{i}}_{lj}$ with $dim(\boldsymbol{g}^{\mathrm{i}}_l) = [N\,x\,1]$
- $\boldsymbol{S}$ with $dim(\boldsymbol{S}) = [N\,x\,N]$
- $\boldsymbol{s}$ with $dim(\boldsymbol{S}) = [N\,x\,1]$
- $\breve{\boldsymbol{\Phi}}, \tilde{\boldsymbol{\Phi}}$ with $dim(\breve{\boldsymbol{\Phi}}, \tilde{\boldsymbol{\Phi}}) = [M\,x\,1]$
- $\breve{\overline{\boldsymbol{q}}}, \overline{\boldsymbol{q}}$ with $dim(\breve{\overline{\boldsymbol{q}}}, \overline{\boldsymbol{q}}) = [M\,x\,1]$
- $\breve{\boldsymbol{H}}, \tilde{\boldsymbol{H}}, \underline{\breve{\boldsymbol{H}}}_{\mathrm{G}}$ with $dim(\breve{\boldsymbol{H}}, \tilde{\boldsymbol{H}}, \underline{\breve{\boldsymbol{H}}}_{\mathrm{G}}) = [M\,x\,M]$
- Infinite beamforming
  1. $\breve{\boldsymbol{\Phi}} = \frac{1}{N^2} \boldsymbol{E}^H \boldsymbol{s}$
  2. $\breve{\boldsymbol{\Phi}} = \breve{\boldsymbol{H}} \tilde{\boldsymbol{\Phi}}_{\mathrm{s}}$
  3. $\breve{\boldsymbol{H}} = \frac{1}{N^2} \boldsymbol{E}^H \boldsymbol{E}$
- $\boldsymbol{\kappa} - \omega$ power transformation
  1. $\tilde{\boldsymbol{\Phi}} = \boldsymbol{E}^H (\boldsymbol{s} \circ \boldsymbol{\Delta} x)$
  2. $\tilde{\boldsymbol{\Phi}} = \tilde{\boldsymbol{H}} \tilde{\boldsymbol{\Phi}}_{\mathrm{s}}$
  3. $\tilde{\boldsymbol{H}} = \boldsymbol{E}^H (\boldsymbol{\Delta} x \circ \boldsymbol{E})$ with $dim(\tilde{\boldsymbol{H}}) = [N_{\mathrm{k}}\,x\,N_{\mathrm{k}}]$
- Conventional beamforming
  1. $\underline{\breve{\boldsymbol{q}}}$ with $\underline{\breve{\eta}}_l = \boldsymbol{g}_l^H \boldsymbol{S} \boldsymbol{g}_l$
  2. $\underline{\breve{\boldsymbol{q}}} = \underline{\breve{\boldsymbol{H}}}_{\mathrm{G}} \underline{\boldsymbol{q}}_{\mathrm{s}}$
  3. $\underline{\breve{\boldsymbol{H}}}_{\mathrm{G}}$ with *rows* $\underline{\breve{\boldsymbol{H}}}_{\mathrm{G|l}} = \boldsymbol{g}_l^H \boldsymbol{G} \boldsymbol{G}^H \boldsymbol{g}_l$

V. Deconvolution

a. The least-squares problem

A deconvolution algorithm is an attempt to calculate a deconvoluted map $\boldsymbol{d}$ from a given dirty map $\boldsymbol{b}$ with known shift-invariant or variant point-spread matrix $\boldsymbol{H}$ by minimizing the least-squares error and introducing a nonnegativity constraint:

$$minimize \quad ||\boldsymbol{b} - \boldsymbol{H}\boldsymbol{d}||^2 \quad \text{subject to} \quad d_m \geq 0 \text{ for all } m \tag{2.104}$$

The deconvolution problem is in general over- or underdetermined, thus an approximate solution can only be found in a least-squares sense by minizing the least-squares error. The same problem arises in linear regression analysis in statistics. A best fit parameter estimation for a defined set of parameters is searched for to model the overdetermined system of linear equation.

A number of deconvolution algorithms was introduced to solve problem (2.104). The algorithms used within this work will be described in the following, starting from shift-invariant algorithms and followed by shift-variant algorithms.

b. Shift-invariant algorithms

Shift-invariant algorithms deal with deconvolution problems that can be formulated as a shift-invariant convolution as follows:

$$\text{minimize} \quad ||\boldsymbol{b} - \boldsymbol{h} * \boldsymbol{d}||^2 \quad \text{subject to} \quad d_m \geq 0 \text{ for all } m \tag{2.105}$$

If the convolution is not shift-invariant one can still apply these algorithms by assuming shift-invariance. Assuming shift-invariance means practically that $\boldsymbol{h}$ is taken as a row vector of all columns in H at row $roundup(\frac{N}{2})$. In that case strong shift-variance leads to especially strong derivations at the boundary region of the underlying source map.

Wiener Deconvolution

The Wiener deconvolution is the least complex deconvolution procedure used within this paper. Developed by Norbert Wiener it is most commonly used in optical image processing.

Idea:

$$\boldsymbol{b} = \boldsymbol{h} * \boldsymbol{d} \Rightarrow \boldsymbol{d} = \boldsymbol{h}^{\mathrm{i}} * \boldsymbol{b} \quad \text{where } \boldsymbol{h}^{\mathrm{i}} \text{ contains the pointwise inverted components of } \boldsymbol{h} \tag{2.106}$$

or in frequency domain

$$\hat{\boldsymbol{b}} = \hat{\boldsymbol{h}}\hat{\boldsymbol{d}} \Rightarrow \hat{\boldsymbol{b}} \circ / \hat{\boldsymbol{h}} = \hat{\boldsymbol{b}} \circ \hat{\boldsymbol{h}}^{\mathrm{i}} = \hat{\boldsymbol{d}} \tag{2.107}$$

Deconvolution through simple inverse filtering is in practice inconvenient due to amplification of background noise. Therefore Wiener additionally included a signal-to-noise ratio dependent filter. Instead of $\hat{\boldsymbol{h}}^{\mathrm{i}}$ one takes the Wiener filter $\hat{\boldsymbol{g}}$ defined most easily in frequency domain as:

$$\hat{g}_l = \frac{1}{\hat{h}_l}\left[\frac{|\hat{h}_l|^2}{|\hat{h}_l|^2 + \frac{1}{s_l}}\right] \tag{2.108}$$

with s_l as the frequency dependent signal to noise ratio. A Wiener filter can be included within DAMAS2 [8] to prevent the amplification of background noise.

DAMAS2 Deconvolution

The DAMAS2 algorithm was developed by Dougherty [8] in an attempt to dramatically increase the deconvolution of sDAS maps by performing fast convolution in frequency space. Fast convolution can only be performed for shift-invariant point-spread functions, thus the shift-variant PSF has to be approximated as shift-invariant by taking only the center PSF. Starting from $\hat{\boldsymbol{b}} = \hat{\boldsymbol{h}_{\mathrm{c}}} * \hat{\boldsymbol{d}}$ one can define the residual $\boldsymbol{r}^i$ of iteration i as:

$$\boldsymbol{r}^i = \boldsymbol{b} - \boldsymbol{h}_{\mathrm{c}} * \boldsymbol{d}^i \tag{2.109}$$

Normalizing with $a = \sum_{j=1}^{N} |h_{\mathrm{c|j}}|$ (for 3 dimensions) one can calculate a new approximation of $\boldsymbol{d}$ by adding the normalized residual to $\boldsymbol{d}^i$:

$$\boldsymbol{d}^{i+1} = \boldsymbol{d}^i + \frac{\boldsymbol{r}^i}{a} \tag{2.110}$$

This is already an iterative algorithm. Non-negativity is ensured by setting $\boldsymbol{d}^i \geq 0$ within each iteration. The DAMAS2 idea is to calculate $\boldsymbol{h} * \boldsymbol{d}^i$ by performing fast-convolution in Fourier space. One gets:

$$\mathcal{F}(\boldsymbol{h} * \boldsymbol{d}^i) = \mathcal{F}(\boldsymbol{h}) \circ \mathcal{F}(\boldsymbol{d}^i) \rightarrow (\boldsymbol{h} * \boldsymbol{d}^i) = \mathcal{F}^{-1}[\mathcal{F}(\boldsymbol{h}) \circ \mathcal{F}(\boldsymbol{d}^i)] \tag{2.111}$$

Therefore one can implement the algorithm in the following steps:

1. Initialize $\boldsymbol{d} = \boldsymbol{d}_0$
2. Calculate $\hat{\boldsymbol{h}_\mathrm{c}} = \mathcal{F}(\boldsymbol{h}_\mathrm{c})$
3. Set $a = \sum_{j=1}^{N} |h_{\mathrm{c|j}}|$
4. Iterate from $i = 1$ till $i = N$
   (a) $\boldsymbol{r}^i = \boldsymbol{b} - \mathcal{F}^{-1}[\hat{\boldsymbol{h}_\mathrm{c}} \circ \mathcal{F}(\boldsymbol{d}^i)]$
   (b) $\boldsymbol{d}^{i+1} = \boldsymbol{d}^i + \frac{\boldsymbol{r}^i}{a}$
   (c) Set $d_l^{i+1} = 0$ if $d_l^{i+1} < 0$

Richardson-Lucy Deconvolution

The Richardson-Lucy Restoration algorithm is an iterative technique for solving the least-squares problem. It is heavily in use for the restoration of astronomical imagery but can also be used for any type of shift-invariant deconvolution problem. It is the most complex algorithm used within this work. Based on an expectation-maximization algorithm it attempts to maximize the likelihood of the deconvolved map. A good explanation can be found in [3]. Original presentations were published as [24] and [20]. It can be performed the following:

1. Set$a = \sum_{j=1}^{N} |h_{\mathrm{c|j}}|$
2. Set $\boldsymbol{d}^0 = \frac{\boldsymbol{b}}{a}$
3. Iterate
   (a) $\boldsymbol{b}^n = \boldsymbol{d}^n * \boldsymbol{h}_\mathrm{c} = \mathcal{F}^{-1}[\mathcal{F}(\boldsymbol{d}^n)\mathcal{F}(\boldsymbol{h}_\mathrm{c})]$
   (b) $\boldsymbol{\epsilon}^n = \boldsymbol{b} \circ / \boldsymbol{b}^n$
   (c) $\boldsymbol{\zeta}^n = \boldsymbol{\epsilon}^n \star \boldsymbol{h}_\mathrm{c} = \mathcal{F}^{-1}[\mathcal{F}(\boldsymbol{\epsilon}^n)\mathcal{F}(\boldsymbol{h}_\mathrm{c}^T)]$
   (d) $\boldsymbol{d}^{n+1} = \frac{1}{a}\boldsymbol{d}^n \circ \boldsymbol{\zeta}^n$

The steps can be explained the following.

1. Initialize normalization parameter
2. Set initial solution
3. Iterate
   (a) Convolve initial solution with centered point spread function to become the estimated dirty map
   (b) Calculate the relative error between estimated and true dirty map
   (c) Correlate the relative error with the centered point spread function (Convolution with the up-down transposed) to get the relative solution error in solution space.
   (d) Update the old solution by weighting it with the relative solution error

The Richardson-Lucy algorithm automatically fulfills the nonnegativity constraint. Energy conservation is additionally fulfilled each iteration as:

$$\sum_{j=1}^{N} d^n = \frac{1}{a} \sum_{j=1}^{N} b_j \tag{2.112}$$

The Richardson-Lucy algorithm can be performed using the *MATLAB* builtin function *deconvlucy*.

c. Shift-variant algorithms

DAMAS Deconvolution

The DAMAS deconvolution algorithm was introduced in 2005 by Brooks and Humphreys ([5]). It has become widely used to deconvolve sDAS maps. It is an iterative algebraic algorithm based on a Gauss-Seidel-type relaxation. The nonnegativity constraint is applied within each iteration.

Writing $\boldsymbol{b} = \boldsymbol{H}\boldsymbol{d}$ in index notation yields

$$\sum_{k=1}^{N} h_{jk} d_k = b_j \tag{2.113}$$

Matrix $\boldsymbol{H}$ contains (eventually) shift-variant point-spread functions $\boldsymbol{h}_j$ for each possible source j, thus, if $\boldsymbol{H}$ is diagonal dominant with $h_{jj} = 1$ one can rewrite (2.113) as

$$b_j = d_j + \sum_{k=1}^{j-1} h_{jk} d_k + \sum_{k=j+1}^{N} h_{jk} d_k \tag{2.114}$$

Note that under- and overrelaxation can be implemented by variation of h_{jj} with scaling factor c as $\boldsymbol{H}' = \frac{\boldsymbol{H}}{c}$. The calculated solution has to be rescaled accordingly as $\boldsymbol{d} = \boldsymbol{d}'c$. It is possible to rearrange (2.114) as

$$d_j = b_j - \sum_{k=1}^{j-1} h_{jk} d_k - \sum_{k=j+1}^{N} h_{jk} d_k \tag{2.115}$$

The problem can be solved by calculating d_j iteratively from $d = 1$ until $d = N$. If the iteration is proceeding from left to right then all d_k at k from $k = 1$ until $j - 1$ were already calculated in the current iteration $n + 1$, while all d_k from$k = j + 1$ until N are available only from the last iteration n.

$$d_j^{n+1} = b_j - \sum_{k=1}^{j-1} h_{jk} d_k n + 1 - \sum_{k=j+1}^{N} h_{jk} d_k^n \tag{2.116}$$

One can define a residual r_j as:

$$r_j^{(n+1)} = d_j^{n+1} - d_j^n = \sum_{k=1}^{j-1} h_{jk} d_k^{(n+1)} + \sum_{k=j}^{N} h_{jk} d_k^{(n)} - b_j \tag{2.117}$$

The new approximation for d_j can be calculated by enforcing the non-negativity constraint

$$d_j^{(n+1)} = max(d_j^{(n)} + r_j^{(n+1)}, 0) \tag{2.118}$$

Known convergence criteria for Gauss-Seidel criteria cannot be applied here due to the additional non-negativity constraint. Due to the successive relaxation scheme convergence may depend on grid point ordering.

Nonnegative Least-Squares

The NNLS algorithm published by Lawson and Hanson [19] in 1987 was one of the first widely used algorithm capable of solving non-negativity constrained least-squares optimisation problems. It is based on a direct minimization of the square sums of $|\boldsymbol{H}\boldsymbol{d} - \boldsymbol{b}|$ using an active set strategy and simple linear regression on the unconstrained set. The problem can be written as

$$min\, \Phi = \frac{1}{2}||\boldsymbol{H}\boldsymbol{d} - \boldsymbol{b}||^2 \quad subject\ to\ d_j \geq 0 \tag{2.119}$$

The gradient of Φ becomes:

$$\boldsymbol{w} = \nabla\Phi = \boldsymbol{H}^T(\boldsymbol{H}\boldsymbol{d} - \boldsymbol{b}) \tag{2.120}$$

Algorithm:

1. Initialization
   (a) Define subset $P = \mathbf{0}$ (passive set) and $R = \boldsymbol{i}$ (active set containing all indices [1,2...M])
   (b) Initialize $\boldsymbol{d} = \mathbf{0}$
   (c) Initialize gradient $\boldsymbol{w} = \boldsymbol{H}^T(\boldsymbol{b} - \boldsymbol{H}\boldsymbol{d})$
2. Main loop
   (a) Take index m of maximal derivative $w_m = max(\boldsymbol{w})$
   (b) Include index m in $\boldsymbol{P}$ and exclude it from $\boldsymbol{R}$
   (c) Calculate the regression vector by including only passive rows of $\boldsymbol{H}$ as $\boldsymbol{s}^{\mathrm{P}} = [(\boldsymbol{H}^{\mathrm{P}})^T\boldsymbol{H}^{\mathrm{P}}]^{-1}(\boldsymbol{H}^{\mathrm{P}})^T\boldsymbol{b}$
   (d) Inner loop (in case the regression vector becomes negativ $min(\boldsymbol{s}^{\mathrm{P}} \leq 0)$)
      i. Calculate the minimal derivative towards the previous solution $\boldsymbol{d}$ as $\alpha = -min[\boldsymbol{d}^{\mathrm{P}} \circ /(\boldsymbol{d}^{\mathrm{P}} - \boldsymbol{s}^{\mathrm{P}})]$
      ii. Calculate a new estimate for $\boldsymbol{d}$ as: $\boldsymbol{d} = \boldsymbol{d} + \alpha(\boldsymbol{s} - \boldsymbol{d})$
      iii. Exclude indices j for $d_j = 0$ (now constrained)from the passive set $\boldsymbol{P}$ and put them in the active set $\boldsymbol{R}$
      iv. Calculate a new regression vector as $\boldsymbol{s}^{\mathrm{P}} = [(\boldsymbol{H}^{\mathrm{P}})^T\boldsymbol{H}^{\mathrm{P}}]^{-1}(\boldsymbol{H}^{\mathrm{P}})^T\boldsymbol{b}$
      v. Ensure the regression vector to be zero at constrained indices : $\boldsymbol{s}^{\boldsymbol{R}} = \mathbf{0}$
   (e) Set $\boldsymbol{d} = \boldsymbol{s}$
   (f) Calculate a new gradient $\boldsymbol{w} = \boldsymbol{H}^T(\boldsymbol{b} - \boldsymbol{H}\boldsymbol{d})$

Chapter 3

Turbulent wall pressure fluctuations

I. The turbulent boundary layer

The following considerations account for fully developed isotropic weakly compressible turbulent boundary layers with zero vertical pressure gradient. Isotropic turbulence can be assumed at sufficiently high Reynolds numbers (generally fulfilled for wind channels) and means that the averaged squared turbulent velocity fluctuations can be assumed constant in all space dimensions.

$$\overline{u'^2} = \overline{v'^2} = \overline{w'^2} \tag{3.1}$$

The principal physical parameters to characterize the macroscopic boundary layer characteristics are:

1. The boundary layer thickness which is (for a turbulent boundary layer) $\delta = \frac{\nu}{U_\infty} 0.14 \frac{Re_x}{\ln Re_x} G(\ln\ Re_x)$
2. The displacement thickness: $\delta_1(x) = \frac{1}{U_\infty} \int_{y=0}^{\infty} (U_\infty - u) dy$ where U_∞ is the upper edge boundary layer velocity and $u(y)$ the horizontal velocity on vertical coordinate y
3. The friction velocity $U_\o = \sqrt{U_\infty / \rho}$
4. The mean wall shear stress $\tau = \rho\nu \frac{\partial u}{\partial y} \sim \rho\nu \frac{U_\infty}{\delta}$ with $\delta = \delta(x, \nu, U_\infty)$

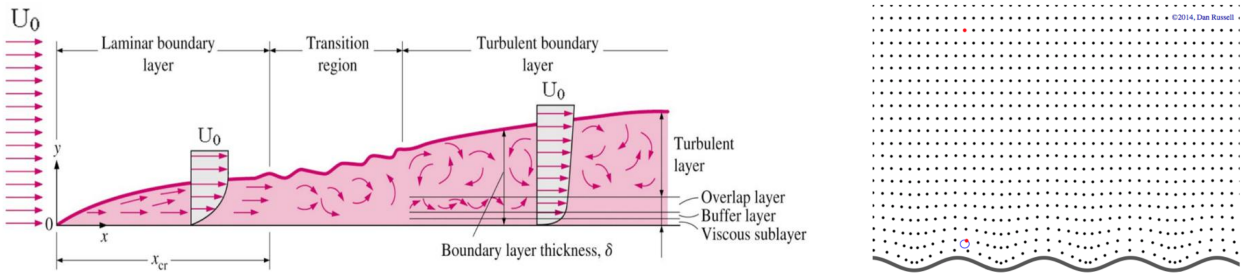

(a) *TBL structure*

(b) *aerodynamic pressure waves*

Fig. 3.1: *Boundary layer structure*

A sketch illustrating the boundary layer development is displayed in Fig. 3.1a. For sufficiently high Reynolds numbers (thus a sufficiently far distance from the frontal edge), the viscous sublayer dominating the laminar boundary layer becomes small compared to the turbulent layer in which fluctuating Reynolds stresses replace the real viscous shear stresses. The transition between the two regions takes place in the buffer region. The

overlap layer is defined above the buffer layer as a region in which both viscous and Reynolds stresses affect the developing velocity distribution.

II. Intuitive explanation

For better understanding of the underlying physics the following part shall serve as an intuitive guide to understand turbulent noise production before the governing equations are derived.

a. Aerodynamic pressure fluctuations (Pseudo-sound)

Aerodynamic pressure fluctuations are caused by macroscopic eddies propagating over the boundary surface. Mathematically negatively turning eddies decrease the near wall flow velocity to fulfill the no-slip condition. The figure shown below 3.1b can be interpreted as a superposition of rotating eddies with a characteristic distance $l_c = \lambda$ reflecting the eddy size. These eddies are propagating with a local convective velocity U_c resulting in an evanescent plane wave. Pressure fluctuations propagating slower than the speed of sound decay rapidly towards flow direction and are called evanescent waves. As their propagation velocity does not match the speed of sound these waves are sometimes referred to as Pseudo-sound.

b. Acoustic pressure fluctuations (sound)

Acoustic pressure fluctuations emerge from free-field turbulent fluctuations as so-called quadrupole noise. This quadrupole noise is related to the fluid elements Reynolds stresses. In case of free flow no forces can act on a single fluid element. Nevertheless, in case of turbulence, velocity fluctuations introduce counteracting forces leading to a local change of vorticity (Fig. 3.2a). Essentially one can describe each of these forces as a dipole source. Superposing the two opposing forces gives the pressure field sketched in Fig. 3.2b. Note that only fluid particles moving at sonic speed can introduce acoustic pressure fluctuations, therefore only a small portion of eddies create sound but this contribution is efficiently transmitted through the medium and therefore dominates the far-field pressure distribution emerging from free-field turbulent eddies. It is important to note that this interpretation of quadrupole noise accounts only for free-field turbulence because the superposition of monopoles is possible only for the homogenous wave-equation (2.17) for which every solution can be expressed as a convolution over Green's function. In case of an enclosing wall the partial differential equation (2.15) has to be solved. It appears that, following the common approach to take into account walls by mirroring, the near-wall source function of quadrupole noise can be expected to be of dipole nature (Fig. 3.1b).

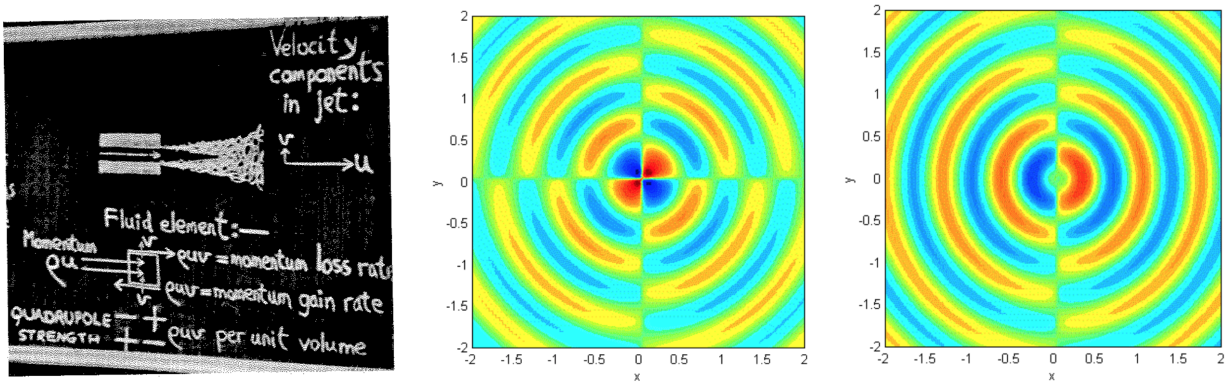

(a) *TBL structure*

(b) *aerodynamic pressure waves*

(c) *Dipole source*

Fig. 3.2: *Aerodynamic pressure fluctuations*

III. Characterization

a. Characterization of aerodynamic turbulent wall pressure fluctuations

Under the assumption of equilibrium flow without mean pressure gradient ∇p and homogeniously distributed turbulence one can describe the pressure field as a distribution of eddies with a range of characteristic lengths l which can directly be related to a range of wavenumbers κ as $l \sim \frac{1}{k_c}$. The dominant contribution of wall-pressures, according to its incompressible nature referred to as aerodynamic contribution, can be interpreted as originating from a 'frozen' pattern of turbulent eddies convected streamwise with local mean flow velocity U_c. These pressure fluctuations decorrelate rapidly due to high mean flow shear stresses as well as turbulent mixing processes. As $l \sim \frac{U_c}{\omega}$ higher frequencies lead to smaller characteristic eddy lengths and small vortices are located closer to the wall they are submitted to slower mean convection velocity (no-slip condition).

Accordingly low frequency contributions can directly be associated with large scale turbulent structures originating from throughout the boundary layer.

In a first attempt to establish a model fulfilling the physical requirements Corcos assumed plane waves propagating with convection velocity U_c experiencing exponential correlation decay in streamwise and lateral direction. Introducing two empirical paramters α and λ reflecting streamwise and lateral correlation lengths, he proposed the famous Corcos model for the shift-invariant cross-power spectral density known as

$$S(\zeta, \omega) = S_{pp}(\omega) e^{k_c \zeta} e^{-i \frac{k_c}{\alpha} |\zeta|} e^{-i \frac{k_c}{\beta} |\eta|}, \tag{3.2}$$

where $k_c = \frac{\omega}{U_c}$ represents the angular wavenumber of convected vortical structures. The corresponding wavenumber-frequency spectrum Φ can be calculated by 2D spatial Fourier transformation obtaining

$$\Phi(\boldsymbol{\kappa}, \omega) = \frac{S_{pp}(\omega)}{\pi^2} \frac{\alpha k_c}{k_c^2 + \alpha^2 (k_1 - k_c)^2} \frac{\beta k_c}{k_c^2 + \beta^2 k_j^2}. \tag{3.3}$$

Theoretical analyses concerning the low wavenumber region were conducted by Kraichnan and Phillips. Their analyses were based on the incompressible Navier-Stokes equation for a plate of infinite extent under statistically stationary turbulence homogenously distributed in plane waves parallel to the wall. Their result became known as the Kraichnan-Phillips theorem stating that $\Phi(\mathbf{0}, \omega) = 0$ [6]. Note that the Corcos-model does not fulfill the Kraichnan-Phillips theorem. The Kraichnan-Phillips theorem became modified as Ffwocs Williams pointed out the importance of supersonic waves by considering compressibility effects and concluding that $\Phi(\boldsymbol{\kappa}, \omega)$ equals zero only if $\boldsymbol{\kappa} = \mathbf{0}$ and $\omega = 0$ but that Φ approaches a non-zero low $\boldsymbol{\kappa}$ limit as $\boldsymbol{\kappa} = \mathbf{0}$. Additionally he estimated the magnitude at $\boldsymbol{\kappa} = \mathbf{0}$ to be proportional to the square of the mean-flow Mach number [6]. The magnitude at $\boldsymbol{\kappa} = \mathbf{0}$ is of great importance because it corresponds to noise radiated orthogonally towards the wall and thus transmitted very efficiently.

b. Characterization of acoustic turbulent wall pressure fluctuations

Theoretical investigations taking into account effects of compressibility are usually based on Lighthills theory of aerodynamic sound. Various approaches (e.g. [25]) predict a non-integratable singularity at the acoustic wavenumber κ_c. The singularity is thought to be related to 'grazing' sound waves with infinite energy density that propagate parallel to the wall. Their origin lies in a theoretically infinitely extensive distribution of turbulent Reynolds stresses. Howe [15] showed that the main mechanisms responsible for a finite sonic contribution are finite boundary-layer size and wall curvature. The two mechanisms are of comparable magnitude and govern the height of the sonic edge. In a simplified approach one can model the cross-power spectral density for an infinite plate as a diffuse field cross-correlation [1]. The diffuse field can be calculated by averaging random incident waves over a halve sphere.

The single plane wave cross-power spectral density can be calculated (see (2.9)) as:

$$S_{pwave}(\zeta, \omega) = \hat{\mathcal{F}} p_1 (\hat{\mathcal{F}} p_2)^* = e^{\kappa r \cos(\theta)} \text{ with } \mathcal{R}(e^{\kappa r \cos(\theta)}) = \cos(\kappa r \cos(\theta)) \tag{3.4}$$

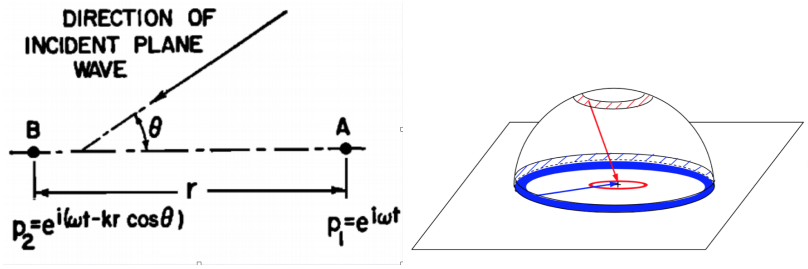

Fig. 3.3: *Diffuse sound field*

Averaging all waves yields:

$$S(\boldsymbol{\zeta},\omega) = S_{\mathrm{pp}}(\omega)\frac{1}{A}\int_{\partial A}\cos(\kappa_0 r\cos(\theta))dA = \frac{S_{\mathrm{pp}}}{4\pi r^2}\int_{\partial A}\cos(\kappa_0 r\cos(\theta))r^2\sin(\theta)d\theta d\phi = \tag{3.5}$$

$$S_{\mathrm{pp}}(\omega)\int_0^{\pi}\int_0^{2\pi}\cos(\kappa_0 r\cos(\theta))\sin(\theta)d\theta\frac{d\theta}{4\pi} = S_{\mathrm{pp}}(\omega)\frac{\sin(\kappa_0|\boldsymbol{\zeta}|)}{\kappa_0|\boldsymbol{\zeta}|} \tag{3.6}$$

The corresponding wavenumber-frequency spectrum becomes

$$\Phi(\boldsymbol{\kappa},\omega) = \frac{S_{\mathrm{pp}}(\omega)}{2\pi k_0^2}\frac{1}{\sqrt{1-(|\boldsymbol{\kappa}|/k_0)^2}} \quad \text{for} \quad |\boldsymbol{\kappa}| \le \kappa_0 \quad \text{and} \quad \Phi = \mathbf{0} \quad \text{for} \quad |\boldsymbol{\kappa}| > \kappa_0. \tag{3.7}$$

c. Simple combined model

Combining (3.2) and (3.7) with a scaling parameter A represents a simplified model reflecting both acoustic and aerodynamic pressure contributions and can be used to evaluate post-processing capabilities for experimental setups [12].

$$S(\boldsymbol{\zeta},\omega) = S_{\mathrm{pp}}(\omega)\frac{1}{1+A}\left[e^{k_{\mathrm{c}}\zeta}e^{-i\frac{k_{\mathrm{c}}}{\alpha}|\zeta|}e^{-i\frac{k_{\mathrm{c}}}{\beta}|\eta|} + A\frac{\sin\kappa_0|\boldsymbol{\zeta}|}{\kappa_0|\boldsymbol{\zeta}|}\right] \tag{3.8}$$

and

$$\Phi(\boldsymbol{\kappa},\omega) = S_{\mathrm{pp}}(\omega)\frac{1}{1+A}\left[\frac{1}{\pi^2}\frac{\alpha k_{\mathrm{c}}}{k_{\mathrm{c}}^2+\alpha^2(k_1-k_{\mathrm{c}})^2}\frac{\beta k_{\mathrm{c}}}{k_{\mathrm{c}}^2+\beta^2 k_{\mathrm{j}}^2} + A\frac{1}{2\pi k_0^2}\frac{1}{\sqrt{1-(|\boldsymbol{\kappa}|/k_0)^2}}\right] \tag{3.9}$$

with $A \neq 0\, for\, |\boldsymbol{\kappa}| \le k_0$ and $A = 0\, for\, |\boldsymbol{\kappa}| > k_0$

d. Model after HOWE

Various authors analytically addressed the problem by taking into account effects of compressibility (e.g. [6]) and derived several different forms of the spectrum. Apparently the wavenumber-frequency spectrum of a uniform homogenous boundary layer of infinite extent on a plane surface in low Mach number flow has a singularity at or near the sonic wavenumber κ_0. This singularity was removed by analytical modifications such as restriction to a finite extent boundary layer, taking account of dissipation of acoustic waves by boundary layer turbulence and the mean-velocity distribution in the TBL led to elimination of the singularity. Therefore the spectrum is expected to have a local finite peak at κ_0. A commonly used model is that given by Chase and modified by Howe

$$\frac{\Phi(\kappa_{\mathrm{x}},\omega)}{\rho^2 U_\tau^3\delta^3} = [(\kappa_+\delta)^2+1/b^2]^{-5/2}\Big(\frac{C_{\mathrm{M}}(\kappa_{\mathrm{c}}^2\delta)\kappa_{\mathrm{x}}^2}{|\kappa_{\mathrm{x}}^2-\kappa_0^2|+\epsilon^2\kappa_0^2} + C_{\mathrm{T}}(\kappa_{\mathrm{x}}\delta)^2\frac{(\kappa_+\delta)^2+1/b^2}{(\kappa_{\mathrm{x}}\delta)^2+1/b^2}\Big(c_1+\frac{c_2|\kappa_{\mathrm{x}}^2-\kappa_0^2|}{\kappa_{\mathrm{x}}^2}+\frac{c_3\kappa_{\mathrm{x}}^2}{|\kappa_2-\kappa_0^2|+\epsilon^2\kappa_0^2}\Big)\Big) \tag{3.10}$$

The variable κ_+ is defined as $\kappa_+ = [(\omega - U_{\mathrm{c}}\kappa_{\mathrm{x}})/(hU_\tau)^2 + \kappa_{\mathrm{c}}^2]$, whereas $b, c_2, c_3, C_{\mathrm{M}}, C_{\mathrm{T}}, h$ are empirical constants. Attempts to gauge these constants rely either on numerical or experimental techniques.

e. Scaling

Collapsing experimental results is a tedious task due to the different turbulent regions associated with different frequency ranges [13]. Note that $\Phi(\omega) = S(\mathbf{0}, \omega)$.The low frequency range for which $\frac{\omega\delta^*}{U_\infty} \leq 0.03$, where δ^* is the boundary layer displacement thickness and U_∞ the free-stream velocity was found to collapse best in the form of $\Phi(\boldsymbol{\omega})\frac{U_\infty}{q_0^2\delta^*}$ as a function of $\frac{\omega\delta^*}{U_\infty}$ where $q_0 = \frac{1}{2}\rho U_\infty^2$ corresponds to the free stream dynamic pressure. Scaling the low frequency range with outer flow variables supports the physical relation to eddy sizes mentioned previously. Various scaling approaches are common in literature for the mid-frequency range $[5 \leq \omega\delta, U_\tau \leq 100]$, where δ is the boundary layer thickness and U_τ is the friction velocity defined as $\sqrt{U_\infty/\rho}$. Scaling on outer flow variables proved beneficial with good collapse if $\Phi(\omega)\frac{U_\tau}{\tau_w^2\delta}$ is plotted over $\frac{\omega\delta}{U_\tau}$. A universal region for which $\Phi(\omega)$ is scale independent and proportional to ω^{-1} represents the passage from medium to high frequencies covering frequencies from $100 \leq \frac{\omega\delta}{U_\infty} \leq 0.3\frac{\delta U_\tau}{\nu}$. Within the universal region $\Phi(\omega)$ yields $\frac{\omega\Phi(\omega)}{\tau_w^2} = const.$. The high frequency range $[\frac{\omega\nu}{U_\tau^2} \geq 0.3]$ collapses best if $\Phi(\omega)\frac{U_\tau^2}{\tau_w^2\nu}$ is plotted as a function of $\frac{\omega\nu}{U_\tau^2}$.

Chapter 4

Evaluation

The performance of the $\boldsymbol{\kappa} - \omega$ power transformation and infinite beamforming deconvolution is analyzed considering a microphone array installed within the main subsonic wind tunnel of Centre Acoustique at École Centrale de Lyon in France. For detailed information concerning the experimental setup see [1]. The array consists of $N = 63$ different microphones aligned along the diameter of a rotating disc. By taking measurements for 63 different angles one arrives at $63\,x\,63 = 3969$ measuring points for the surface. The pressure signals were recorded for $90s$ at each angle. Afterwards the cross-power spectral density $S(\zeta, \eta, \omega)$ was computed using the Welch periodogram method with a sampling frequency of $25.6kHz$ and averaging over 400 data blocks of $0.08s$ with 50% overlap. Note that the resulting spectrum covers only distances in the upper halfspace $\zeta+, \eta\pm$. The property of conjugate-symmetry allows to calculate the lower halfspace $\zeta-, \eta\pm$ cross-power spectral density S^- as the conjugate of S^+.

For validation a mixed diffuse-corcos model with a convective-acoustic power ratio of $r = 0.01$ (or $20dB$) is simulated as analysis input. Two different grids are applied to evaluate the presented algorithms on different regions. The first region covers the whole range of possible wavenumbers while the second region is centered around the acoustic region. The large grid covers the domain from $\kappa_{\mathrm{x}_{\min}} = -100[\frac{1}{m}]$ until $\kappa_{\mathrm{x}_{\max}} = 800[\frac{1}{m}]$ and from $\kappa_{\mathrm{y}_{\min}} = -800[\frac{1}{m}]$ until $\kappa_{\mathrm{y}_{\max}} = 800[\frac{1}{m}]$ with a resolution of $\Delta\kappa = 5[\frac{1}{m}]$. The small grid covers a rectangular area ranging from $\kappa_{\mathrm{x}_{\min}} = -120[\frac{1}{m}]$ until $\kappa_{\mathrm{x}_{\max}} = 120[\frac{1}{m}]$ and respective in κ_{y} with a resolution of $\Delta\kappa = 2[\frac{1}{m}]$. The full procedure is explained using the algorithms derived in previous sections. Afterwards deconvolution results are compared for both algorithms.

I. Calculation

For application of DAS or the $\boldsymbol{\kappa} - \omega$ transform the following input data is provided:

- Matrices $\boldsymbol{\zeta}$ and $\boldsymbol{\eta}$ with components ζ_{mn} and η_{mn} defining a grid of N possible separation vectors
- Matrices $\boldsymbol{K}_{\mathrm{x}}$ and $\boldsymbol{K}_{\mathrm{y}}$ with components $\kappa_{\mathrm{x}|\mathrm{op}}$ and $\kappa_{\mathrm{y}|\mathrm{op}}$ defining a grid of L focus wavenumbers
- Matrice $\boldsymbol{S}$ with components s_{mn} corresponding to each possible separation vector ζ_{mn} and η_{mn}

Now by assigning a unique index j to each possible separation distance and cross-power spectral density matrix index pair mn and similarly a unique index l to each focus wavenumber index pair op one can define the steering matrix $\boldsymbol{E}$ with components $e_{jl} = e^{i(\kappa_{\mathrm{x}|l}\zeta_j + \kappa_{\mathrm{y}|l}\eta_j)}$ and the cross-power spectral density vector $\boldsymbol{s}$. Let Z and M denote the number of possible separation distances and focus wavenumbers respectively.

a. Beamforming

A beamforming map can easily be calculated from shift-invariant cross-power spectral density matrices as explained in (2.81).

$$\breve{\boldsymbol{\Phi}} = \frac{1}{Z}\boldsymbol{E}^H \boldsymbol{s} \tag{4.1}$$

Note that N^2 was replaced by Z. $Z = N^2$ holds only if multiple identical correlations for the same separation vector are stored, which is computationally ineffective. Thus the resulting amount of possible separation distances is $Z \leq N^2$.

The full point spread matrix $\breve{\boldsymbol{H}}$ is necessary only for shift-variant deconvolution algorithms (here: DAMAS, NNLS). For shift-invariant deconvolution algorithms it is sufficient to provide only the point-spread function resulting from a single source of strength 1 at the center of the region of interest. $\breve{\boldsymbol{H}}$ can be calculated as

$$\breve{\boldsymbol{H}} = \frac{1}{Z}\boldsymbol{E}^H \boldsymbol{E} \tag{4.2}$$

whereas the centered point-spread vector for a single source situated at index l_c, the so-called convolution kernel, calculates as:

$$\breve{\boldsymbol{h}}_\mathrm{c} = \frac{1}{Z}\boldsymbol{E}^H \boldsymbol{E}(l_\mathrm{c}, :) \tag{4.3}$$

Mention that it is possible to calculate $\breve{\boldsymbol{H}}$ from $\breve{\boldsymbol{h}}_\mathrm{c}$ using the shift-invariance property.

b. The wavenumber-frequency transformation

The $\boldsymbol{\kappa} - \omega$ transformation is calculated as shown in (2.85). Additionally, instead of the conventional rectangular window, a hamming window is included to reduce spectral leakage. The resulting map $\tilde{\boldsymbol{\Phi}}$ becomes:

$$\tilde{\boldsymbol{\Phi}} = \frac{1}{(2\pi)^2}\boldsymbol{E}^H(\boldsymbol{s} \circ \boldsymbol{\Delta}x \circ \boldsymbol{w}_\mathrm{hanning}) \tag{4.4}$$

The full-point spread matrix $\tilde{\boldsymbol{H}}$ becomes (following (**??**))

$$\tilde{\boldsymbol{H}} = \frac{1}{(2\pi)^2}\boldsymbol{E}^H(\boldsymbol{\Delta}x \circ \boldsymbol{w}_\mathrm{hanning} \circ \boldsymbol{E}) \tag{4.5}$$

with centered point-spread vector

$$\tilde{\boldsymbol{h}}_\mathrm{c} = \frac{1}{(2\pi)^2}\boldsymbol{E}^H(\boldsymbol{\Delta}x \circ \boldsymbol{w}_\mathrm{hanning} \circ \boldsymbol{E}(l_\mathrm{c}, :).') \tag{4.6}$$

Note that $\boldsymbol{\Delta}x$ and $\boldsymbol{w}_\mathrm{hanning}$ denote row-vectors in case (4.4) and (4.6) but an M-column matrix with vectors $\boldsymbol{\Delta}x$,$\boldsymbol{w}_\mathrm{hanning}$ respectively in case (4.5).

c. Energetical normalization

In order to fulfill Parseval's theorem it is important to normalize point-spread vector $\tilde{\boldsymbol{h}_\mathrm{c}}$ and matrix $\tilde{\boldsymbol{H}}$ with $e_0 = \sum_{l=1}^{M} h_{\mathrm{c}|\mathrm{l}}$ as

$$\tilde{\boldsymbol{h}_{0\mathrm{c}}} = \frac{\tilde{\boldsymbol{h}_\mathrm{c}}}{e_0} \quad \textit{and} \quad \tilde{\boldsymbol{H}}_0 = \frac{\tilde{\boldsymbol{H}}}{e_0} \tag{4.7}$$

Energetical normalization is meaningful only for the $\boldsymbol{\kappa} - \omega$ transformation.

II. Analytical result

Analytical results are shown for large and small grid as analytically described in Chapter 3 are shown in Fig. 4.1a and Fig. 4.1b. All following plots shown for evaluation reasons are scaled relative to the map absolute value in linear scale from 0 [blue] to 1[red].

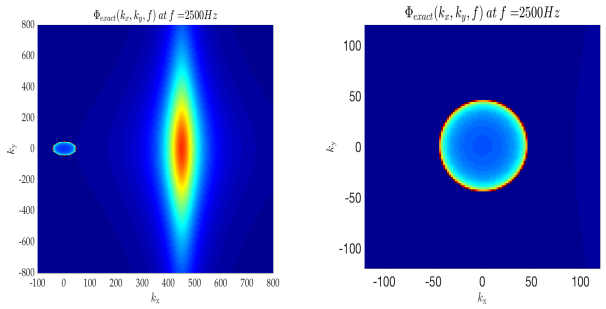

(a) *Total spectrum* **(b)** *Acoustic contribution*

Fig. 4.1: *Analytical result*

III. Comparison iBEAM deconvolution

The problem is calculated on the large grid using DAMAS2 and RL. These are the only algorithms capable of solving for the fine grid containing 181 *x* 321 nodes. Afterwards all four presented algorithms are evaluated on the small grid containing 121 *x* 121 nodes.

a. Large grid

The conventional infinite beamforming map (iBEAM) shown in Fig. 4.2a roughly allows to identify convective ridge and acoustic region. The convective region is blown up in width and generally overestimates the presence of incoming waves. The sonic region is strongly underestimated and no circular edge can be detected. The iBEAM point-spread function shown in Fig. 4.2b (on the small grid) is not accurately resolved at the current resolution of $\Delta\kappa = 5\frac{1}{m}$. Regarding the different deconvolution algorithms it is shown in Fig. 4.2c (DAMAS2) that the convective region intensity is strongly reduced at the cost of a vanishing acoustic region whereas the Richardson-Lucy algorithm (Fig. 4.2d) performs much better in conserving the general shape but still underestimates the size of the acoustic region. No sonic region can be detected.

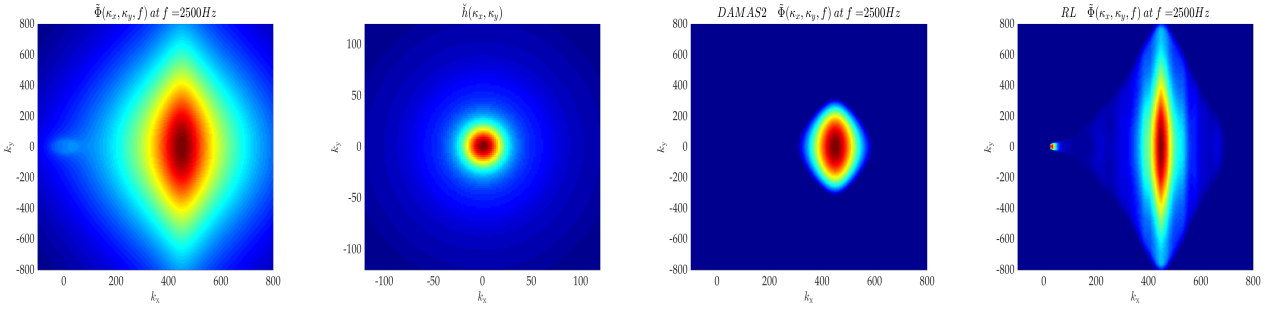

(a) **(b)** **(c)** **(d)**

Fig. 4.2: *iBEAM deconvolution large grid*

A coarse point-spread function resolution is assumed as the main reason for the bad results obtained on the large grid. Finer resolution is not an appropriate solution due to high computational effort , especially as the

convective ridge is moving rightwards at higher frequencies. Additionally convergence is more difficult to obtain for grids containing a large number of nodes. Instead the small grid is tested.

b. Small grid

A major drawback of this grid can be seen in Fig. 4.4b. The presence of strong contributions of energy at the domain border is disadvantageous considering that the real sources lie to a big part outside the considered domain. Thus the resulting problem is especially ill-posed meaning that no source distribution within the considered region can actually satisfy the dirty map (Fig. 4.3).

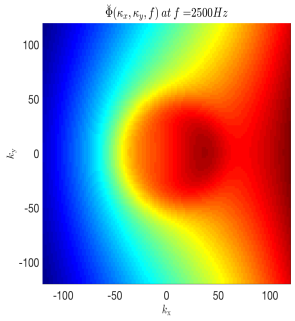

Fig. 4.3: *Dirty map iBEAM*

The different deconvolution results are shown in Fig. 4.4.The DAMAS algorithm is capable of removing most lobes showing a recognizable sonic region. Vertical lobes at the right corner result from the strong contribution of energy coming from the convective region. DAMAS2 shows only a single peak around the acoustic-wavenumber in the right halve-space. The Richardson-Lucy algorithm also succeeds in detecting the sonic region but the result is horizontally clinched and not homogenous. NNLS shows a distribution of single peaks with a slightly increased energy distribution around the sonic region. Neither algorithm is satisfying, thus leading to the implementation of $\boldsymbol{\kappa} - \omega$ deconvolution as shown in the following.

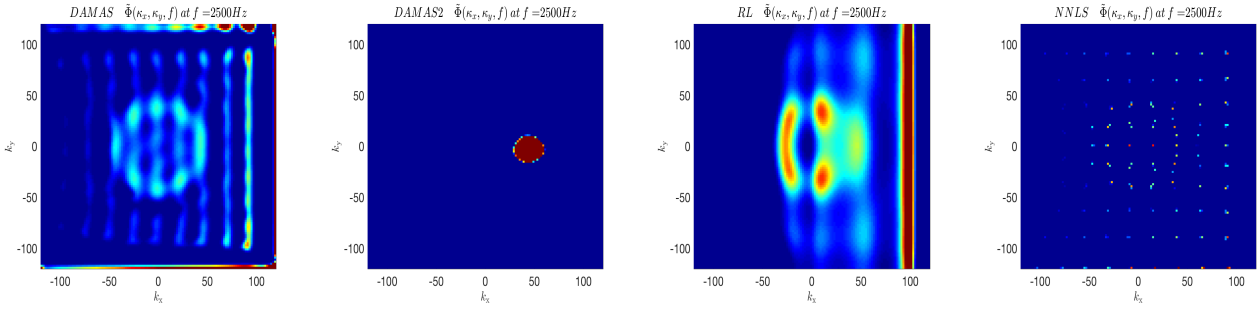

(a) **(b)** **(c)** **(d)**

Fig. 4.4: *iBEAM deconvolution for small grid*

IV. Comparison $\kappa - \omega$ power deconvolution

a. Large grid

The nonequidistantly-spaced $\boldsymbol{\kappa} - \omega$ power transform shown in Fig. 4.5a is quite close to the analytical result. Beams resulting from the convolution of the underlying source distribution with point-spread function (Fig. 4.5b) results in only small lobes towards higher values of κ_x. The sonic-region is well-defined but underestimated in comparison with the hydrodynamic ridge. The presence of a single lobe around $\boldsymbol{\kappa} = \mathbf{0}$ is probably caused by the convolution of the circular sonic region with a circular point-spread function, resulting in a strong superposition of lobes in the center. Application of DAMAS2 (see Fig. 4.5c) succeeds in eliminating the high-wavenumber lobes as well as the central lobe. As a backdraw the low-energy subconvective waves disappear. Application of Richardson-Lucy does not yield any convergent results.

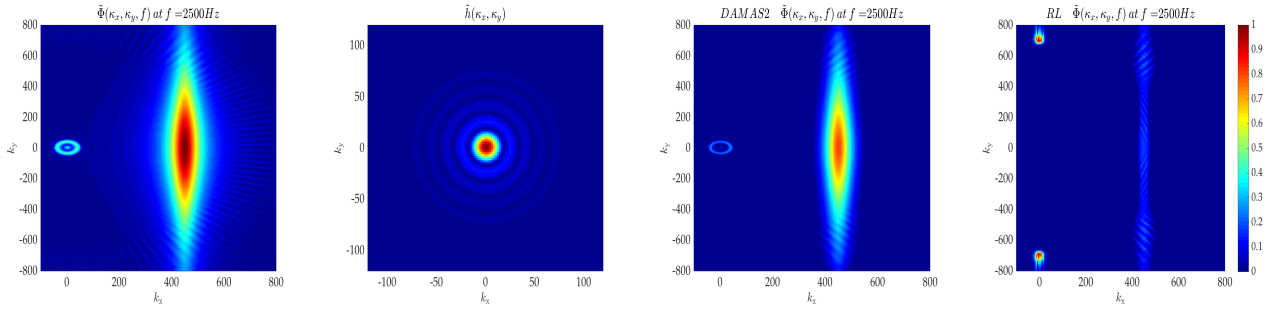

Fig. 4.5: $\boldsymbol{\kappa} - \omega$ *power deconvolution large grid*

b. Small grid

One of the biggest advantages of $\boldsymbol{\kappa} - \omega$ power transformation in comparison with iBEAM is the more distinct separation between convective and acoustic region. Fig. 4.6 shows a very well resolved diffuse field with almost all energy concentrated correctly within the acoustic region. The map is thus much better defined than the small DAS map and allows for better deconvolution performance.

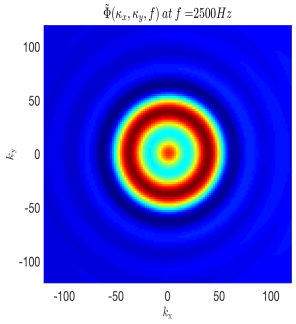

Fig. 4.6: $\boldsymbol{\kappa} - \omega$ *power transformation*

Each deconvolution algorithm succeeds in detecting the sonic region. DAMAS shows equidistantly distributed spots at the sonic region and is the only algorithm capable of reducing the relative center lobe energy. DAMAS2 is able to correctly extract the acoustic region boundary although the resulting energy distribution is not totally homogenous. The Richardson-Lucy algorithm shows a very well resolved homogenous sonic region. Although the center-lobe could not be reduced it is deemed the best result for the acoustic region so far. NFFT shows an inconvenient distribution of spots around the sonic region.

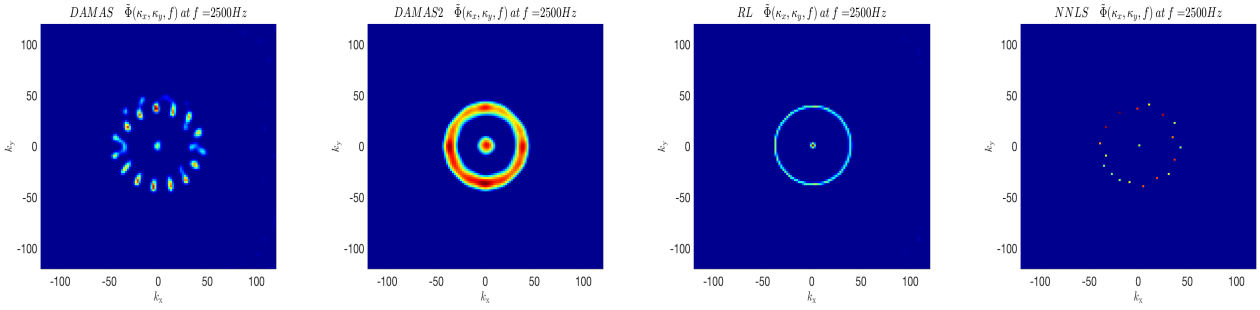

Fig. 4.7: $\boldsymbol{\kappa} - \omega$ *power deconvolution small grid*

No deconvolution algorithm is capable of preserving energy. Although the Richardson-Lucy algorithm is energy preserving it does so only if a normalization common in image processing is used which is not yet applied [10].Thus, the deconvolution output is rescaled as :

$$\tilde{\mathbf{\Phi}}^{\mathrm{D}} = \frac{\tilde{\mathbf{\Phi}}^{\mathrm{D}}}{\sum_{l=1}^{M} \tilde{\Phi}_l^{\mathrm{D}}} \sum_{l=1}^{M} \tilde{\Phi}_l \tag{4.8}$$

Comparing the analytical result, the $\boldsymbol{\kappa} - \omega$ power transformation and the rescaled RL deconvolved map (Fig. 4.8) one can draw the following conclusion:

- The sonic region is much better defined in the RL deconvolved map although slightly shifted inwards from the real sonic wavenumber $\kappa_0 = 46[\frac{1}{m}]$
- The energy at $\boldsymbol{\kappa} = \mathbf{0}$ is strongly overestimated in comparison with the original $\boldsymbol{\kappa} - \omega$ power transformation

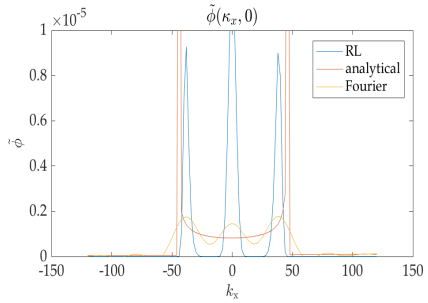

The deconvolution does not seem to be an appropriate attempt to detect numerically correct values within the acoustic region but it greatly enhances the visibility of the high energy sonic edge. It is thus deemed a valuable tool to scan wavenumber-frequency spectra for the numerically predicted sonic region.

Fig. 4.8: *quantiative performance RL $\boldsymbol{\kappa} - \omega$ deconvolution*

V. Conclusion

The following conclusions are drawn from evaluating the different algorithms:

1. The quality of measured spectra can be increased by applying the DAMAS2 algorithm on the $\boldsymbol{\kappa} - \omega$ power transformation
2. The visibility of a potential sonic region can be strongly increased by applying the Richardson-Lucy algorithm on a $\boldsymbol{\kappa} - \omega$ power power transformation on the acoustic region

Chapter 5

Experimental results

The experimental data was post-processed as previously evaluated for the analytical testcase and is shown as a function of outer flow variables $\tilde{\Phi}(\frac{\omega\delta^*}{U_\infty})$. Applying the DAMAS2 algorithm on the $\boldsymbol{\kappa}-\omega$ transformation of the $50\frac{m}{s}$ ($M = 0.13$) zero pressure gradient case shown in Fig. 5.1a yields that the estimated underlying source field displayed in Fig. 5.1b has considerably stronger concentration of energy around the center of the aerodynamic ridge than previously predicted. The lobes polluting the whole region are efficiently removed outside the primary regions while some remaining lobe structures are still visible in the aerodynamic region. A strong contribution at $\boldsymbol{\kappa} = \mathbf{0}$ is detected. The nature of this contribution is not yet clear but it is assumed to stem from strong orthogonally impinging waves due to boundary layer reflection or possibly also duct modes.

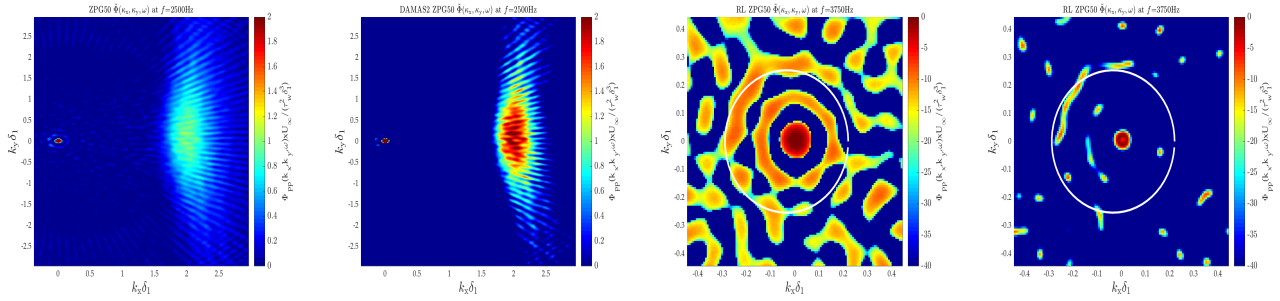

(a) $\boldsymbol{\kappa}-\omega$ *transformed spectrum (big grid)* **(b)** $\boldsymbol{\kappa}-\omega$ *deconvolved spectrum (big grid)* **(c)** $\boldsymbol{\kappa}-\omega$ *transformed acoustic spectrum (small grid)* **(d)** $\boldsymbol{\kappa}-\omega$ *deconvolved spectrum (small grid)*

Fig. 5.1: *Comparison spectrum at* $f = 2500Hz$ *,*$M = 0.13$

Analyzing the acoustic Richardson-Lucy deconvolved spectrum for different frequencies (Fig. 5.2) reveals that the strong contribution at $\boldsymbol{\kappa} = \mathbf{0}$ preveals at all frequencies. Some maps at higher frequencies suggest the dominance of contributions around the ellipse reflecting the dispersion relation as for $f = 3750Hz$ (Fig. 5.1d) but in general accordance is not sufficient to claim the existence of the sonic ridge. It has to be pointed out that the maps are shown in a strongly dynamic scale covering 4 orders of magnitude relativ to the maximal map value. Effectiveness of the $\boldsymbol{\kappa}-\omega$ deconvolution procedure is demonstrated by comparing the spectrum obtained through $\boldsymbol{\kappa}-\omega$ power transform of $S(\boldsymbol{\zeta},\omega)$ (Fig. 5.1c) and the spectrum obtained through subsequent application of a deconvolution procedure (Fig. 5.1d).

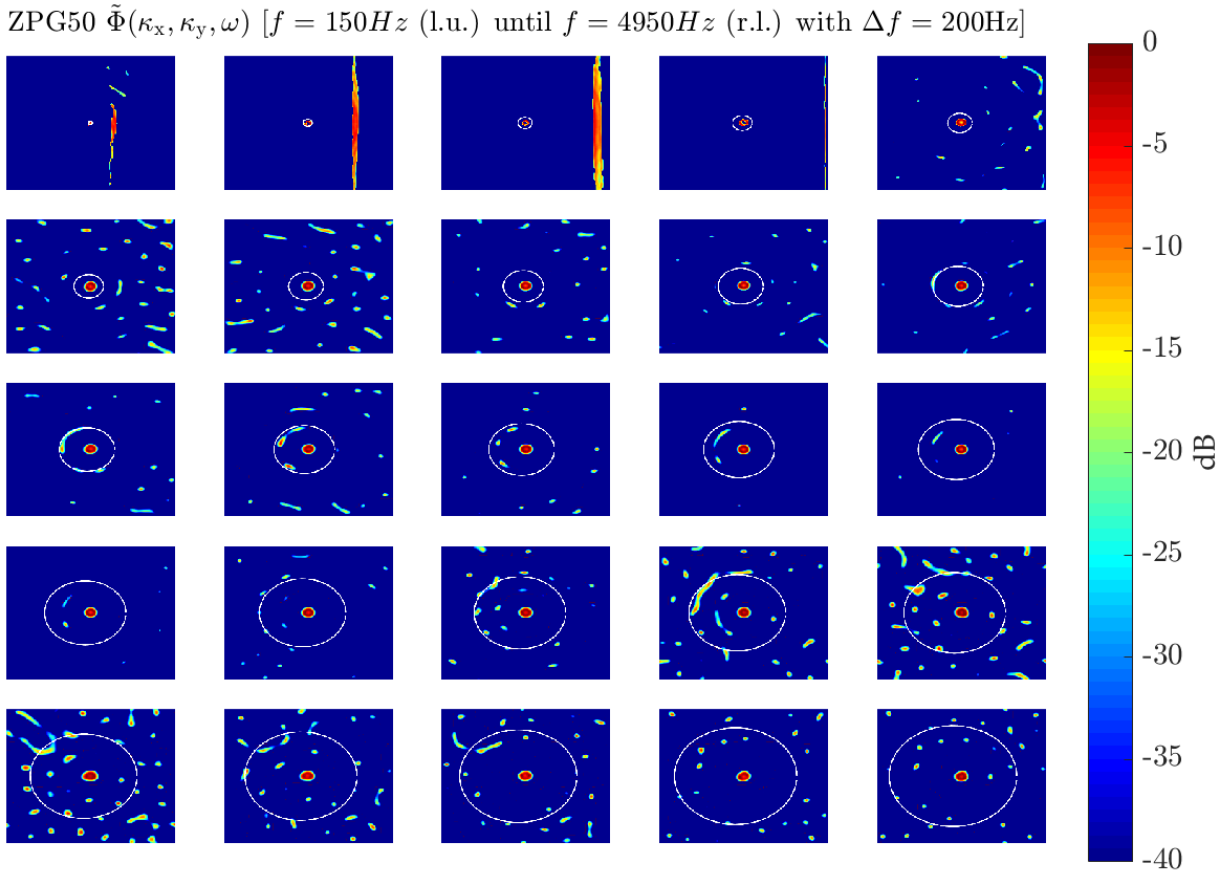

Fig. 5.2: $\boldsymbol{\kappa} - \omega$ *deconvolved acoustic spectrum* $M = 0.13$

More interesting deductions can be drawn for a velocity of $75\frac{m}{s}$ ($M = 0.23$). As for the previous case energy becomes concentrated in the core of the aerodynamic ridge. But by looking at the deconvolved acoustic spectrum for different frequencies (Fig. 5.4) one can clearly identify strong contributions around the sonic edge. The orthogonal component at $\boldsymbol{\kappa} = \mathbf{0}$ is still present but reduced in power. It seems as if the sonic contributions are stronger in the negative wavenumber region which is especially interesting by pointing out that the microphone array is rotating and the shift-invariant cross-power spectrum does not depend on the absolute microphone position. As a result the concentration does not seem to be related to disturbing directional noise in the measuring process but to be either a feature of boundary layer noise or a result from errors in signal processing which is not probable. It is emphasized that the obtained results are the first measurements of the acoustic contribution of turbulent boundary layer wall pressure fluctuations for low Machnumbers ever observed. By applying an inverse Fourier transformation of the deconvolved wavenumber-frequency spectrum one obtains a least-squares trigonometric interpolation of the pure acoustic cross-power spectral density (Fig. 5.5). The spatial maps cover maximal correlation lengths of $l_c = \pm\frac{2\pi}{\Delta\kappa} = \pm\frac{2\pi}{2} = \pm 3.14m$. An estimation of correlation lengths higher than the array diameter $D = 0.25m$ is possible because the cross-power spectral density is assumed to be a solution of

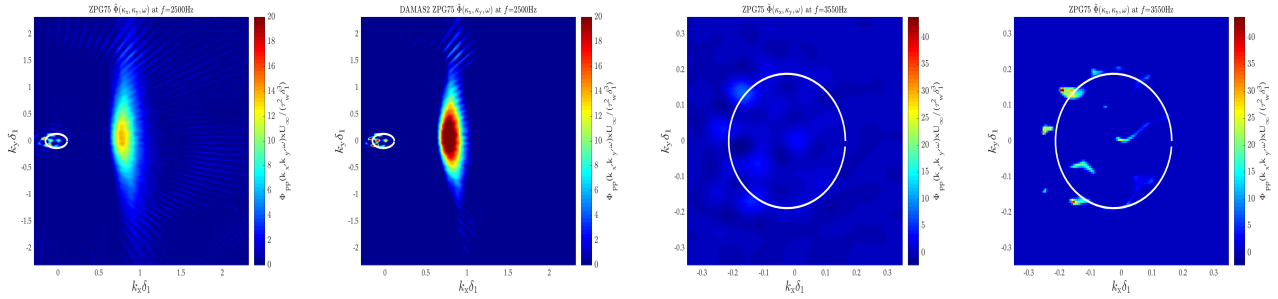

(a) $\kappa - \omega$ *transformed spectrum (big grid)* **(b)** $\kappa - \omega$ *deconvolved spectrum (big grid)* **(c)** $\kappa - \omega$ *transformed acoustic spectrum (small grid)* **(d)** $\kappa - \omega$ *deconvolved spectrum (small grid)*

Fig. 5.3: *Comparison spectrum at* $f = 2500Hz$, $M = 0.23$

the Helmholtz equation and thus orthogonality is approximately true for every focus wavenumber (restricted by array size) and by applying a deconvolution procedure one can theoretically predict every wave as long as Nyquist's criteria is fulfilled. Thus even very low wavenumbers corresponding to high correlation lengths can be obtained. The low-frequency maps show strong correlation for long separation distances in mean flow direction. Mid-frequency cross-spectra show direction independent correlation lengths as expected for the acoustic diffuse field while those for higher frequencies seem to show strongest correlations for separation vectors not aligned with the mean flow. The appearance of a favorable direction of propagation that is not aligned with the mean flow comes unexpected and can not yet be explained.

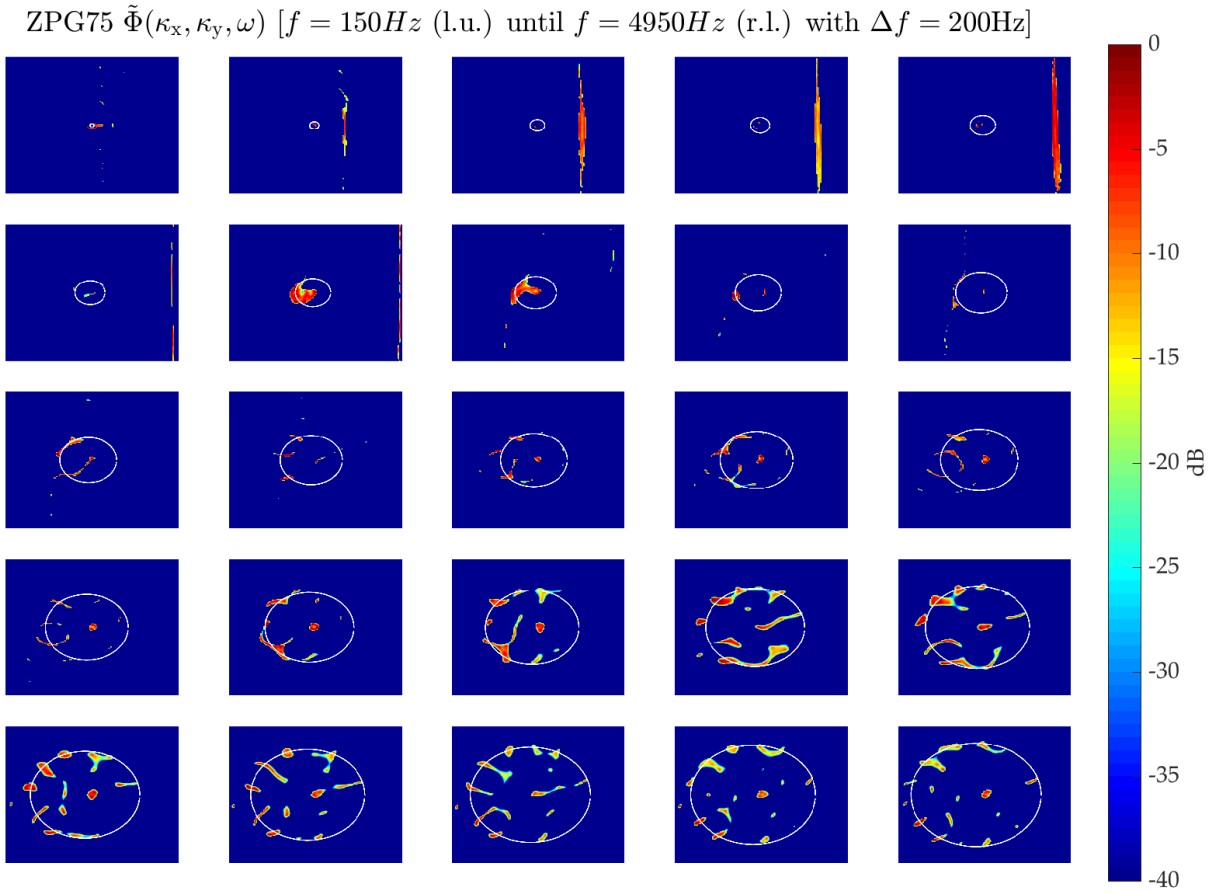

Fig. 5.4: $\boldsymbol{\kappa} - \omega$ *deconvolved acoustic spectrum* $M = 0.23$

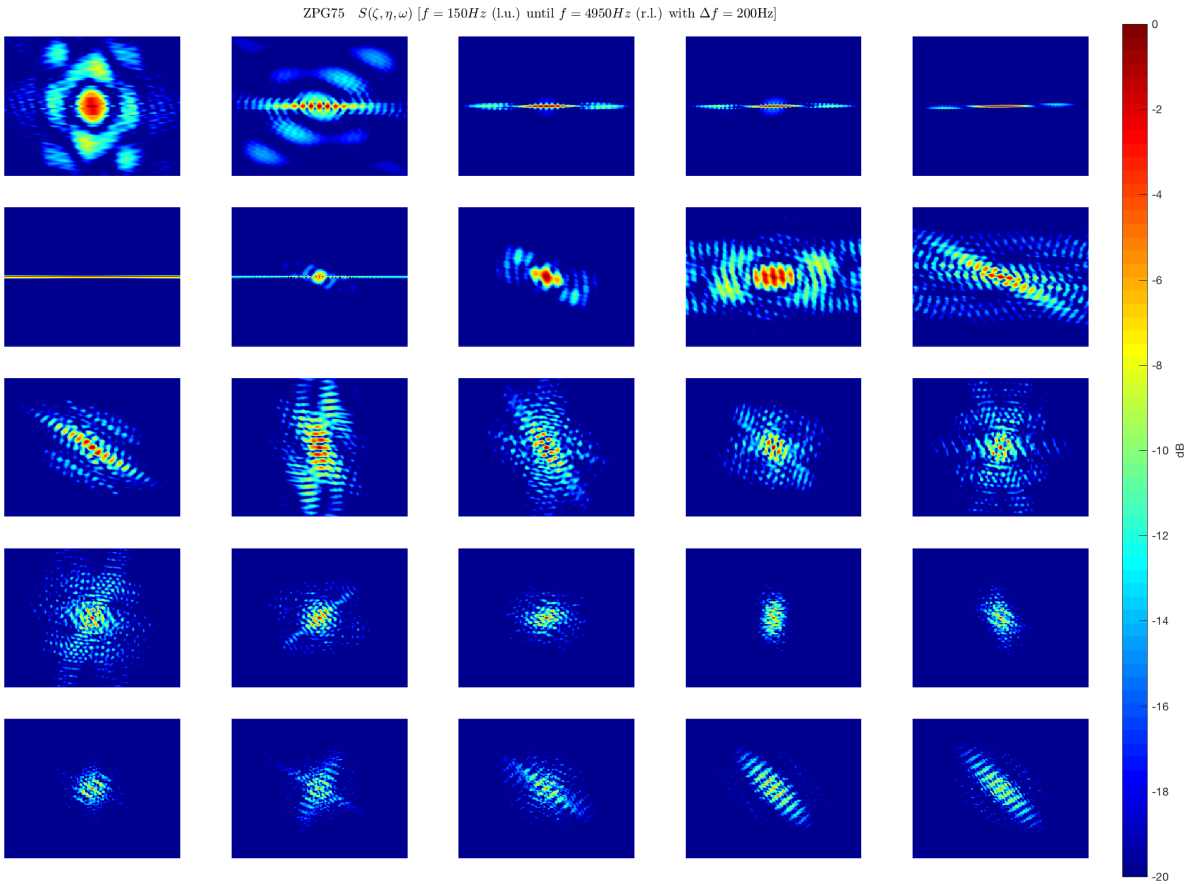

Fig. 5.5: *Spatial least-squares trigonometric interpolation of acoustic cross-spectrum* $M = 0.23$

I. Summary

The previous work has been focused on the signal processing necessary to estimate the interior noise contribution underneath a homogenous TBL over a flat plate. For that purpose previous experimental work on 2D arrays was analyzed and a new approach was developed to improve the resulting wavenumber-frequency spectrum. By analyzing the infinite beamforming approach chosen by Ehrenfried et al. [11] and by deriving its relation to the Fourier transform it became clear that, especially for the low-wavenumber region, a non-equidistant Fourier transform is better suited to reproduce and measure the spectrum. Infinite beamforming might still be a well-suited algorithm to access convected wall-pressure fluctuations underneath strong background noise because the correlations between microphones of small distance are weighted the same as those for long correlations (contrary to the spatial weighting using the $\boldsymbol{\kappa} - \omega$ transformation). Application of functional beamforming might help in identifying small wavenumber contributions but the resulting spectrum is no longer directly related to the Fourier transform and can therefore not be convolved with the structural response to estimate the resulting interior noise. The tremendously high amount of microphones necessary for experimental validation is not realizable in practice which results in a coarse microphone response that distorts the underlying spectrum. The true spectrum can be estimated by applying deconvolution algorithms that solve the corresponding non-negative least-squares problem. For this purpose a range of modern deconvolution algorithms was applied on an analytical model and the Richardson-Lucy algorithm emerged as the most well-suited one. Nevertheless the obtained spectra are only a single solution of the potentially non-unique least-squares problem and therefore have to be treated with care. Following the successful validation on a simple convective-acoustic model the process has been applied on experimental data obtained from low Mach number measurements on a rotating array at École Centrale de Lyon. At $M = 0.23$ the resulting spectrum weakly indicates the expected sonic ridge while strong orthogonally impinging waves of unknown origin dominate the wavenumber-frequency spectrum at $M = 0.13$.

II. Outlook

The study of TBL wall pressure fluctuations that has been the driver of this work remains an extraordinary challenge for the future years to come. Despite the decades of years of research that have already been spent core goals like a reasonable estimate for the direct acoustic pressure contribution underneath a homogenous TBL on a flat plate remain unclear. The ever-mounting power and accessability of high performance computing might allow numerical computations to gain access to this important quantity within the near future but its experimental proof might still take its time. The measuring setup necessary to be able to separate the small acoustic contribution from the strong hydrodynamic one demands extraordinary sophistication. Even more challenging is the calculation of interior noise emanating from the non-homogenous TBL developing over complex geometries, which is a major area of interest for especially automotive and aeronautic industries. The calculation and storage of the (measured or simulated) cross-power spectral density for 2D geometries over the whole frequency range is itself an obstacle that grows tremendously (from 2D to 4D) if neither shift-invariance nor symmetry can be assumed. In case a clear and sound wavenumber-frequency representation is found for a range of dimensionless inner and outer flow variables engineers will be able to adopt, correct and develop the analytical models to extract the essential variables that govern the driving turbulent mechanisms. When that time has come new geometries and structures can be developed to design a new generation of low noise cars and aircrafts that as a result allow to push the various performance limits currently restrained by excessive noise development.

Bibliography

[1] Bailly C. Robert G. Arguillat B., Ricot D. Measured wavenumber-frequency spectrum associated with acoustic and aerodynamic wall pressure fluctuations. *J. Acoustc. Soc.*, 128(4):1647–55, Oct 2010.

[2] Chris Bahr. Wavespace-based coherent deconvolution. *NASA Langley Research Center,Hampton, VA 23681*.

[3] Mark Biggs, David S. C. ; Andrews. *Acceleration of iterative image restoration algorithms*, volume 36(8),p.1766. Applied Optics, 1997.

[4] P. G. Bremner and J. F. Wilby. Aero-vibro-acoustics: Problem statement and methods for simulation-based design solution. *AIAA Paper*, (2001-01-1629).

[5] T.F. Brooks and W.Humphreys. A deconvolution approach for the mapping of acoustic sources (damas) determined from phased microphone arrays. *Paper 2004-2954, AIAA*, 10th AIAA/CEAS Aeroacoustics Conference, May 2004.

[6] M. K. Bull. Wall-pressure fluctuations beneath turbulent boundary layers: Some reflections on forty years of research. *Journal of Sound and Vibration*, 190(3):299–315, 1996.

[7] E. Guyader C. Cacciolati, P. Neple. Comparison of the vibroacoustic behaviour of a rectangular thin plate excited by a diffuse sound field and a turbulent boundary layer. *Proceedings of ICSV 13*, 2006.

[8] R.P. Dougherty. Extension of damas and benefits and limitations of deconvolution in beamforming. *Paper 2005-2961, AIAA*, 4th AIAA/CEAS Aeroacoustics Conference, Toulouse, France, June 1998.

[9] Washington D.C. Earl G. William, Naval Research Laboratory. Fourieracoustics, sound radiation and nearfield acoustical holography. 1999.

[10] Klaus Ehrenfried and Lars Koop. *A comparison of iterative deconvolution algorithms for the mapping of acoustic sources*. German Aerospace Center DLR, 2006.

[11] Klaus Ehrenfried and Lars Koop. *Experimental study of pressure fluctuations beneath a compressible turbulent boundary layer*. German Aerospace Center DLR, 2008.

[12] E. Salze et al. Investigation of the wall pressure wavenumber-frequency spectrum beneath a turbulent boundary layer with pressure graadient. In *International Symposium on turbulence and Shear Flow Phenomena (TSFP-9)*, 2015.

[13] Theodore M. Farabee. Spectral features of wall pressure fluctuations beneath turbulent boundary layers. *Phys. Fluids A 3*, 10, 1991.

[14] Xavier Gloerfelt. *The link between wall pressure spectra and radiated sound from turbulent boundary layers*. Arts et Métiers ParisTech,DynFluid Laboratory, 2010.

[15] M. S. Howe. On the structure of the turbulent boundary-layer wall pressure spectrum in the vicinity of the acoustic wavenumber. *Proc. R. Soc. Lond. A*, 412:389–401, 1987.

[16] M. S. HOWE. Surface pressures and sound produced by turbulent flow over smooth and rough walls. *Journal of the Acoustical Society of America 95, 1041–1047*, 1991.

[17] J.J.Christensen and J.Hald. *Technical Review Beamforming*, volume No.1. Brüel and Kjaer, 2004.

[18] Manfred Kaltenbacher. *Skriptum zur Vorlesung Strömungsakustik (TU Wien)*. March 2015.

[19] C.L. Lawson and R.J. Hanson. Solving least squares problems. *Prentice-Hall,Englewood Cliffs,NJ*, 1974.

[20] L. B. Lucy. *An iterative technique for the rectification of observed distributions*, volume 79(6):745-754. Astronomical Journal, 1974.

[21] E. Mollo-Christensen M. T. Landahl. *Turbulence and Random Processes in Fluid Mechanics*, volume 2. Cambridge, 1992.

[22] Brad Osgood. *EE261 The Fourier Transform and its Application*.

[23] Robert W. Pratt. The interpretation of space-time spectral quantities. *Journal of the atmospheric sciences*, 33:1060–1066, 1976.

[24] W.H.Richardson. *Bayesian-based iterative method of image restoration*, volume 62(1):55-59. Journal of the Optical Society of America, 1972.

[25] Ffowcs Williams. Surface-pressure fluctuations induced by boundary-layer flow at finite mach number. *J. Fluid Mech.*, 22:507–5019, 1965.